

2016


Dynamics of Plume-Triple Junction Interaction: Results from a Series of Three-Dimensional Numerical Models and Implications for the Formation of Oceanic Plateaus

Mladen Dordevic

Jennifer Georgen

Old Dominion University, jgeorgen@odu.edu

Follow this and additional works at: https://digitalcommons.odu.edu/oeas_fac_pubs

 Part of the [Geochemistry Commons](#), and the [Geophysics and Seismology Commons](#)

Repository Citation

Dordevic, Mladen and Georgen, Jennifer, "Dynamics of Plume-Triple Junction Interaction: Results from a Series of Three-Dimensional Numerical Models and Implications for the Formation of Oceanic Plateaus" (2016). *OEAS Faculty Publications*. 214. https://digitalcommons.odu.edu/oeas_fac_pubs/214

Original Publication Citation

Dordevic, M., & Georgen, J. (2016). Dynamics of plume-triple junction interaction: Results from a series of three-dimensional numerical models and implications for the formation of oceanic plateaus. *Journal of Geophysical Research: Solid Earth*, 121(3), 1316-1342. doi:10.1002/2014jb011869

RESEARCH ARTICLE

10.1002/2014JB011869

Key Points:

- A series of dynamic models investigates mantle plume–triple junction interaction
- Variations in oceanic plateau area, bathymetry, and crustal thickness are calculated
- Models offer a framework for constraining plateau formation in natural settings

Correspondence to:

J. Georgen,
jgeorgen@odu.edu

Citation:

Dordevic, M., and J. Georgen (2016), Dynamics of plume–triple junction interaction: Results from a series of three-dimensional numerical models and implications for the formation of oceanic plateaus, *J. Geophys. Res. Solid Earth*, 121, 1316–1342, doi:10.1002/2014JB011869.

Received 7 JAN 2015

Accepted 19 JAN 2016

Accepted article online 22 JAN 2016

Published online 11 MAR 2016

Dynamics of plume–triple junction interaction: Results from a series of three-dimensional numerical models and implications for the formation of oceanic plateaus

Mladen Dordevic^{1,2} and Jennifer Georgen³

¹Department of Physics, Old Dominion University, Norfolk, Virginia, USA, ²Now at Incorporated Research Institutions for Seismology, Washington, District of Columbia, USA, ³Department of Ocean, Earth, and Atmospheric Sciences, Old Dominion University, Norfolk, Virginia, USA

Abstract Mantle plumes rising in the vicinity of mid-ocean ridges often generate anomalies in melt production and seafloor depth. This study investigates the dynamical interactions between a mantle plume and a ridge–ridge–ridge triple junction, using a parameter space approach and a suite of steady state, three-dimensional finite element numerical models. The top domain boundary is composed of three diverging plates, with each assigned half-spreading rates with respect to a fixed triple junction point. The bottom boundary is kept at a constant temperature of 1350°C except where a two-dimensional, Gaussian-shaped thermal anomaly simulating a plume is imposed. Models vary plume diameter, plume location, the viscosity contrast between plume and ambient mantle material, and the use of dehydration rheology in calculating viscosity. Importantly, the model results quantify how plume-related anomalies in mantle temperature pattern, seafloor depth, and crustal thickness depend on the specific set of parameters. To provide an example, one way of assessing the effect of conduit position is to calculate normalized area, defined to be the spatial dispersion of a given plume at specific depth (here selected to be 50 km) divided by the area occupied by the same plume when it is located under the triple junction. For one particular case modeled where the plume is centered in an intraplate position 100 km from the triple junction, normalized area is just 55%. Overall, these models provide a framework for better understanding plateau formation at triple junctions in the natural setting and a tool for constraining subsurface geodynamical processes and plume properties.

1. Introduction

1.1. Plume-Ridge Interactions

Hot spots and mid-ocean ridges are the surface expressions of subsurface mantle upwelling and magma generation processes. At mid-ocean ridges, lithospheric plates diverge and the mantle upwells, creating the oceanic crust through decompressional melting. Hot spots are typically associated with elevated topography or shallow bathymetry and often also with linear volcanic chains showing systematic age progression of the eruptive products. It is widely believed that many hot spots are associated with mantle plumes [e.g., Morgan, 1971, 1972, 1981; Detrick *et al.*, 2002; Ito *et al.*, 2003; Putirka *et al.*, 2007; Wolfe *et al.*, 2009; Leroy *et al.*, 2010; Barruol and Fontaine, 2013]. A mantle plume is commonly defined as a region of the mantle that is hotter than the surrounding material, originating from convective thermal boundary instabilities [Olson, 1990]. Geochemical heterogeneity has also been suggested to be important in plume dynamics and upwelling. The interaction of mantle plumes with nearby mid-ocean ridges results in physical and chemical anomalies along 15–20% of the total mid-ocean ridge system length [Ito *et al.*, 2003]. Based upon the spatial extent of bathymetric swells and magnetic isochron data, it can be shown that plume-ridge interactions may last for several million years or longer [e.g., Cannat *et al.*, 1999; Ito *et al.*, 2003].

Previous authors have established scaling laws for plume-ridge dynamical interaction and tested them against experimental data obtained either in the lab using corn syrup tanks [e.g., Feighner and Richards, 1995] or using solutions from numerical models [Ribe *et al.*, 1995; Ribe, 1996; Ito *et al.*, 1996, 1997; Albers and Christensen, 2001]. For example, early studies [e.g., Feighner and Richards, 1995] found a relationship between plume volume flux (Q), half-spreading rate (u), and waist width (W , the length of ridge axis influenced by a

dispersing mantle plume): $W = c(Q/u)^{1/2}$, where c is a constant. This relatively simple relationship has been further developed and refined by subsequent modeling studies [e.g., Ito *et al.*, 1997; Ribe and Delattre, 1998; Albers and Christensen, 2001], but it captures an essential inverse proportionality between spreading rate and waist width. That is, for a plume of a given flux, the slower a ridge's spreading rate, the longer the ridge axis that is expected to show plume-related anomalies.

1.2. Triple Junctions

A triple junction is defined as a point where three plate boundaries meet [McKenzie and Morgan, 1969]. Triple junctions represent important geological settings along the global mid-ocean ridge system where mantle dynamics are influenced by the motions of three plates. Each branch of a triple junction can be a ridge, trench, or transform fault, resulting in 16 basic possible configurations, of which only some are stable over geologic time [McKenzie and Morgan, 1969]. From the velocity vector method it can be shown that ridge-ridge-ridge (RRR) triple junctions are stable for all possible spreading rates and ridge orientations. Several previous studies [e.g., Sclater *et al.*, 1976; Searle, 1980; Searle and Francheteau, 1986; Mitchell and Parson, 1993; Klein *et al.*, 2005; Miranda *et al.*, 2014] have investigated plate kinematics and the geological characteristics of the seafloor near RRR triple junctions.

1.3. Study Objectives: Plume–Triple Junction Interactions

The primary objective of this investigation is to improve understanding of the dynamics of plume–triple junction interaction. A series of numerical models is used to assess the role of RRR plate divergence in governing the dispersion of plume material in the upper mantle. The models vary multiple parameters, including the location of the plume with respect to the triple junction, plume flux, and mantle viscosity structure. The results from these numerical models provide insight into the generation of oceanic plateaus at RRR triple junctions.

To our knowledge, this is the first numerical study that systematically investigates plume–triple junction interaction using a series of geodynamical models. As such, a major goal of this work is to explore, in the general sense, how plate boundary geometry affects plume advection and plume-related seafloor anomalies. Before the modeling is applied to any specific plume–triple junction system, it is important to develop understanding about how various parameters interplay to affect the dynamics of the system. Therefore, this manuscript is structured to first present and discuss the results of the series of numerical models. Then examples are provided to show how the modeling methodology can be applied to specific geological settings.

1.4. Prior Geodynamic Studies: RRR Triple Junctions

Previous studies [e.g., Georgen and Lin, 2002; Georgen, 2008; Georgen and Sankar, 2010; Georgen, 2011] have used numerical modeling to explore generalized properties of mantle flow and thermal patterns in the vicinity of RRR triple junctions. Georgen and Lin [2002] investigated the case of a slower spreading ridge quasi-orthogonally intersecting two nearly collinear faster-spreading ridges. The mantle was assumed to be an incompressible, isoviscous fluid driven by the diverging surface plates. Heat was exchanged via advection and diffusion, and no source of buoyancy was included. The divergence rates of the plates were changed by a fixed scaling factor to simulate the half-spreading rates of three extant triple junctions: the Azores triple junction in the Atlantic Ocean, in which the most rapidly diverging ridge is ultraslow spreading; the Rodrigues triple junction in the Indian Ocean, in which the most rapidly diverging ridge is intermediate spreading; and the Galapagos triple junction in the eastern Pacific Ocean, in which the most rapidly diverging ridge is fast spreading. The study found that the flow patterns of the faster-spreading, collinear ridges were not significantly influenced by the presence of the triple junction. On the other hand, upwelling velocities along the axis of the slowest ridge were enhanced as much as threefold toward the triple junction. This effect was strongest for a triple junction where the fastest opening ridge was slow spreading. With linear multiplicative increase of the spreading rates for all three ridges, the presence of the triple junction had less influence on the flow patterns of the slowest ridge.

Georgen [2008] investigated a plate boundary configuration similar to the Rodriguez triple junction. This work focused mainly on the mantle dynamics of the slowest-spreading ridge, and it incorporated pressure- and temperature-dependent mantle viscosity. Results were significantly quantitatively different from the isoviscous case [Georgen and Lin, 2002], with estimated increases in upwelling velocity and along-axis flow up to 100 km away from the triple junction. Within a few hundred kilometers of the triple

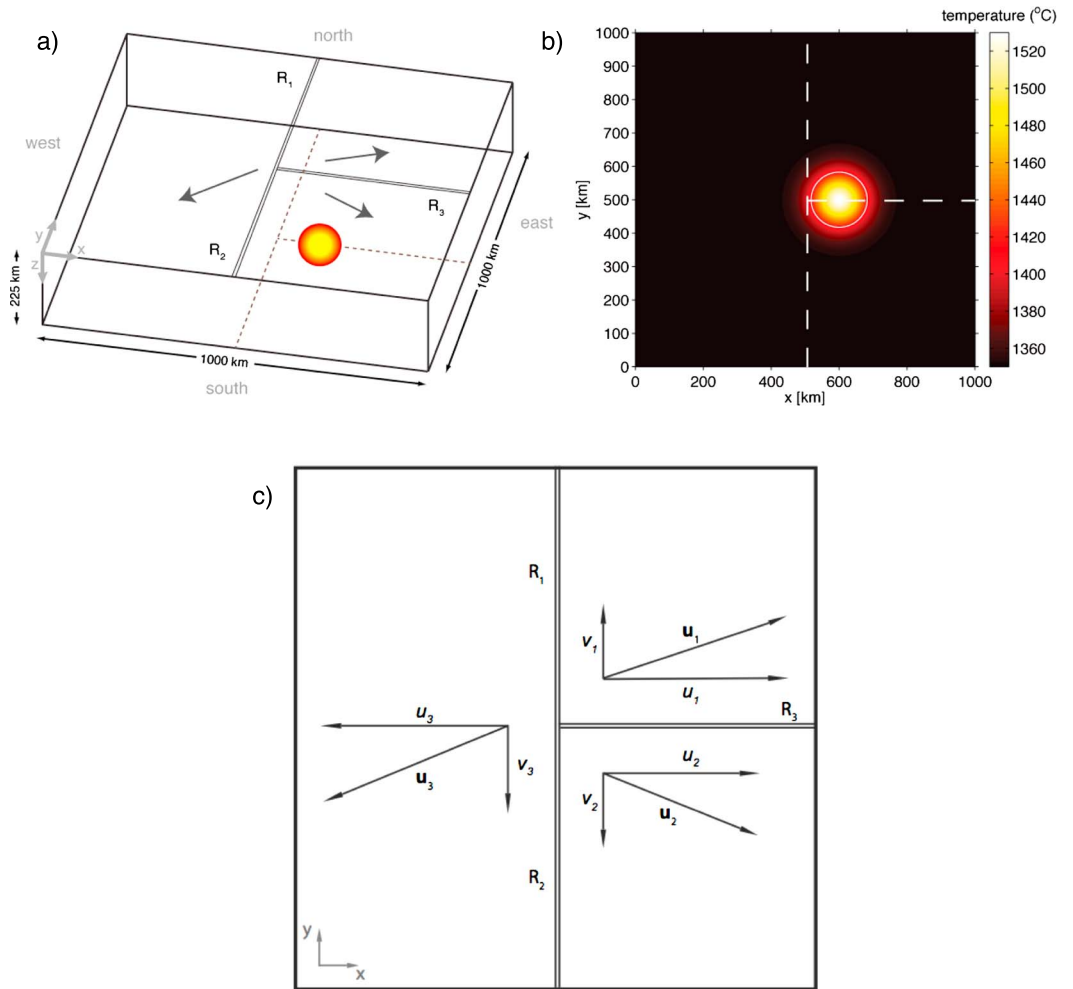


Figure 1. (a) Computational domain representation. Three plates diverge from a triple junction located at ($x = 500$ km, $y = 500$ km). R_1 and R_3 are the fastest-spreading and slowest-spreading ridge branches, respectively. On the bottom boundary, the circle marks a plume conduit with a location along R_3 . Dashed lines are projections of the top plate boundaries onto the bottom of the model domain, for reference. (b) Assigned temperature field on the bottom boundary of the model domain. The plume source is simulated with a thermal anomaly field with maximum excess temperature ΔT . The excess temperature decreases away from the center of the plume source in a radial fashion according to a Gaussian function, to approach ambient mantle temperature. The plume diameter is defined using the standard deviation of the Gaussian function (see text for additional details); white circle shows extent of plume defined in this manner. (c) Top plate velocities relative to triple junction. Values for plate velocities can be found in Table 1.

junction, temperatures at a depth within the partial melting zone increased by 40°C and the crust thickened about 1 km.

Georgen and Sankar [2010] focused on the Azores Plateau and Azores triple junction, and specifically on geodynamical processes along the model analogue of the ultraslow-spreading Terceira Rift. By incorporating a discontinuity that simulated the nearby Gloria Fracture Zone, diffuse deformation near the three ridges' intersection, and time-dependent spreading history, *Georgen and Sankar* [2010] explored additional factors that could affect crustal accretion around the Azores triple junction. An overall conclusion of this study was that although plate boundary geometry may contribute to melting patterns around the Azores triple junction to some degree, a mantle heterogeneity is likely necessary to explain the full extent of anomalous magmatism.

The interaction of a mantle plume with a triple junction was studied by *Georgen* [2011]. To explore the effects of the triple junction on plume dispersion, this investigation compared the results of two numerical models. In one model, a plume interacted with three diverging boundaries. In the other model, the plume retained the

Table 1. Plate Motion Vectors Assigned to Top Boundary of Model Domain

Component	Value (cm/yr)
$ \mathbf{u}_1 $	1.265
u_1	1.205
v_1	0.400
$ \mathbf{u}_2 $	1.078
u_2	1.000
v_2	-0.400
$ \mathbf{u}_3 $	1.307
u_3	-1.205
v_3	-0.501

same assigned properties and location, but divergence was set to zero along the branch simulating the Terceira Rift. Unlike the second model, the first model predicted preferential flow along the Terceira Rift and the portion of the Mid-Atlantic Ridge to the south of the triple junction, in general qualitative agreement with observations of asymmetric plume dispersion along the ridge system [Dosso *et al.*, 1993; Detrick *et al.*, 1995; Thibaud *et al.*, 1998; Goslin and Triatnord Scientific Party, 1999; Vogt and Jung, 2004; Maia *et al.*, 2007].

This investigation differs from earlier geodynamical studies in several important respects. Most significantly, unlike Georgen [2011] which used only one set of plume parameters, this study calculates between 100 and 200 models to systematically investigate the dynamics of plume-triple junction interaction under a variety of conditions. Second, in a subset of the suite of models, this investigation uses viscosity that is dependent on mantle dehydration upon melting, in addition to pressure- and temperature-dependent viscosity. As discussed below, the use of dehydration rheology has a significant effect on calculated patterns of plume dispersion.

2. Numerical Methods and Model Description

2.1. General Overview of Model Domain

The physical system is described by an incompressible fluid layer that is confined in between two parallel, horizontal surfaces (Figure 1a). The top surface is divided into three diverging plates to simulate spreading ridges with prescribed opening rates (Figure 1c and Table 1). The temperature of the top plate is held constant at T_c ; the temperature of the bottom plate is T_h ($T_h > T_c$), on top of which is added a two-dimensional thermal anomaly field simulating the plume source (Figure 1b). The center of the thermal anomaly is assigned a specific location and maximum excess temperature ΔT . Excess temperature is prescribed to decrease away from the center point of the thermal anomaly according to a Gaussian function. The size of the region with temperature that is elevated over ambient mantle temperature is controlled by specifying a standard deviation length. The bottom-heated fluid rises buoyantly, transferring heat toward the top plate. Small changes of the density across the fluid relative to the ambient density are ignored except in the buoyancy force term in the momentum equation, where they are directly proportional to temperature. This approximation is known as the Boussinesq approximation of Rayleigh-Benard convection.

2.2. Governing Equations

This three-dimensional numerical modeling investigation calculates steady state solutions for mantle flow using the finite element software package COMSOL [e.g., Georgen and Sankar, 2010; Georgen, 2011]. COMSOL has been benchmarked with several other codes for a subduction zone model [van Keken *et al.*, 2008]. The numerical models solve the heat advection-diffusion equation with the incompressible Navier-Stokes equations:

$$\nabla \cdot \mathbf{u} = 0 \quad (1)$$

$$\rho \mathbf{g} = -\nabla \cdot [\eta(p, T) \nabla \mathbf{u}] + \rho(\mathbf{u} \cdot \nabla) \mathbf{u} + \nabla p \quad (2)$$

$$\kappa \nabla^2 T = \mathbf{u} \cdot \nabla T \quad (3)$$

In these equations, \mathbf{u} is velocity vector, T is temperature, \mathbf{g} is gravitational acceleration, κ is thermal diffusivity, ρ is density, p is pressure, and $\eta(p, T)$ is pressure- and temperature-dependent viscosity. Values for material properties and parameters are listed in Table 2. Mantle density is temperature dependent such that

$$\rho = \rho_m(1 - \alpha(\Delta T)) \quad (4)$$

Table 2. Model Parameters

Variable	Meaning	Value	Units
A	Dehydration parameter	1, [1, 50]	
d	Plume diameter	[125, 165]	km
E	Activation energy	2.5×10^5	J/mol
F	Body force		N
g	Gravitational acceleration	9.81	m/s^2
p	Pressure	Pa	
r	Radial distance of the plume from triple junction	[50, 75, 100]	km
R	Universal gas constant	8.314	J/mol K
T	Temperature		K
T_h	Temperature at bottom boundary without thermal anomaly	1350	$^{\circ}C$
T_c	Temperature at top boundary	0	$^{\circ}C$
ΔT	Mantle plume excess temperature	180	$^{\circ}C$
\mathbf{u}	Velocity vector		cm/yr
u, v, w	x, y, z components of \mathbf{u}		cm/yr
V	Activation volume	4×10^{-6}	m^3/mol
x	Distance in direction parallel to slowest-spreading ridge axis		km
y	Distance in direction perpendicular to slowest-spreading ridge axis		km
z	Depth below surface		km
α	Coefficient of thermal expansion	3×10^{-5}	K^{-1}
η_o	Minimum ambient viscosity	10^{19}	Pa s
η_{max}	Maximum cutoff viscosity	10^{21}	Pa s
η_{min}	Minimum cutoff viscosity	5×10^{18}	Pa s
θ	Azimuth of the plume relative to R_1	[90, 135, 180, 225, 270, 315]	deg
κ	Thermal diffusivity	1	mm^2/s
ρ	Density		kg/m^3
ρ_o	Reference mantle density	3300	kg/m^3
ρ_w	Reference water density	1030	kg/m^3
ρ	Reference crustal density	2700	kg/m^3

For numerical simplicity, standard normalized and nondimensional forms of the above equations are solved. The dimensionless Rayleigh number appears in the nondimensionalized form of the governing equations. The Rayleigh number is

$$Ra = [g\alpha\rho_o(T_h - T_c)h^3]/(\kappa\eta_o) \quad (5)$$

where h is a length scale and ρ_o and η_o are reference mantle density and viscosity (discussed below), respectively. The Rayleigh number describes the tendency of a fluid to convect.

2.3. Numerical Domain and Boundary Conditions

This system of equations is solved within a Cartesian box of dimensions 1000 km \times 1000 km \times 225 km (Figure 1a). Guided by earlier studies [Georgen and Sankar, 2010; Georgen, 2011], the horizontal ($x - y$) extent of the domain was chosen to capture distribution of the plume material along 500 km for each ridge. Previous authors [Ito et al., 1999; Hall and Kincaid, 2003] investigating plume-ridge interactions used maximum domain depths corresponding with the upper mantle transition zone. They found that the majority of the plume-lithosphere interaction occurred in the upper 200 km of the domain. Therefore, this study uses a maximum depth of 225 km to save computational time. The domain was discretized into rectangular prism elements so that grid spacing ranged from 12.5 km to 35 km. The lowest grid spacing is near the ridges and the plume, and it extends from the top boundary of the model domain to the bottom boundary. Results obtained by the same models computed using a coarser resolution produced comparable results. To ensure that the size of the numerical domain was sufficient to prevent edge effects from contaminating the region of interest (i.e., the area of plume-triple junction interaction), the results of a series of models with different domain sizes and similar numerical grids were compared.

On the top surface of the domain, the positions of the ridges and triple junction are fixed. Triple junction geometry displays a general tendency to take either a "T" or a "Y" shape [Georgen and Lin, 2002]. Examples of the former include the present-day Rodrigues, Azores, and Galapagos triple junctions, and examples of the latter

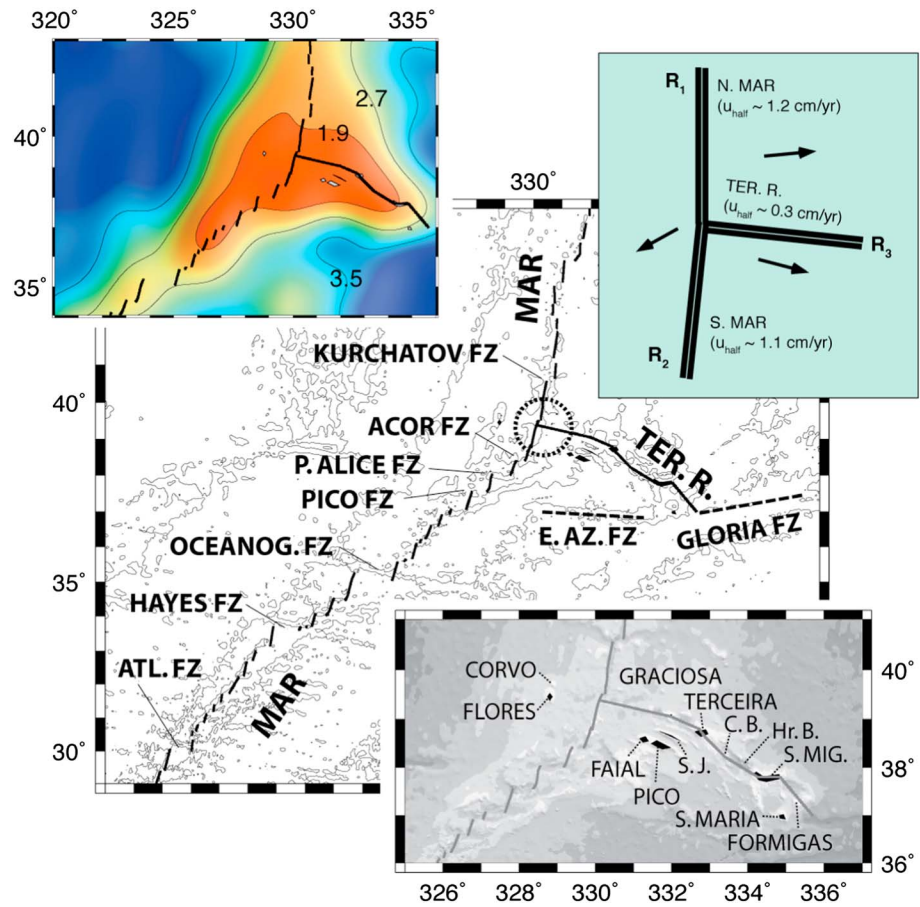


Figure 2. Figure modified from *Georgen* [2011]. (center) Geological setting of the Azores. Dashed circle marks the position of the Azores triple junction. Abbreviations MAR, TER. R., and E. AZ. FZ are Mid-Atlantic Ridge, Terceira Rift, and East Azores Fracture Zone, respectively. (left inset) Filtered bathymetry of the Azores plateau. A low-pass filter with a cutoff wavelength of 300 km was applied to the bathymetry data of *Smith and Sandwell* [1997]. Contour lines mark 1.9, 2.7, and 3.5 km isobaths. (bottom right inset) Islands in the Azores Archipelago. Abbreviations S. J., S. Mig., C. B., and Hr. B. are Sao Jorge Island, Sao Miguel Island, Castro Bank, and Hirondelle Basin, respectively. (top right inset) Schematic representation of the Azores triple junction. Black arrows indicate direction of plate motions relative to the triple junction.

are the present-day Bouvet triple junction and the Pacific-Izanagi-Farallon triple junction in the Jurassic-Cretaceous Pacific, which is associated with the formation of the large igneous province Shatsky Rise [*Sager et al.*, 1988; *Nakanishi et al.*, 1999]. To build upon and extend earlier work [*Georgen and Sankar*, 2010; *Georgen*, 2011], this investigation models a T-shaped triple junction with spreading rates similar to the Azores (Figure 2). Ultraslow-spreading ridge R_3 intersects two faster-spreading ridges R_1 and R_2 at a right angle (Figure 1). Plate divergence vectors, calculated assuming a fixed triple junction, were determined from *Luis et al.* [1994] and *Luis and Miranda* [2008] (Table 1). For each of the three plate motion vectors, taking the components of the vector perpendicular to the adjacent ridge axes yields half-spreading rates similar to those of the present-day Azores triple junction.

The vertical sides of the model domain are set to be insulated walls with no shear stress:

$$-\hat{n} \cdot \nabla T = 0 \tag{6}$$

$$\eta (\nabla \mathbf{u} + (\nabla \mathbf{u})^T) \cdot \hat{n} = 0 \tag{7}$$

The bottom boundary is set as an open boundary with normal stress being zero:

$$[-p\mathbf{l} + \eta (\nabla \mathbf{u} + (\nabla \mathbf{u})^T)] \cdot \hat{n} = 0 \tag{8}$$

As described in the previous paragraph, two-dimensional (x and y) velocity components are assigned to each point on the top surface of the model domain, to simulate the divergence of three plates away from a fixed triple junction point. On the top surface, the vertical (z) component of velocity is set to zero.

The bottom boundary is kept at a constant temperature T_h except in the area assigned a superimposed Gaussian-shaped temperature anomaly that represents a mantle plume. The treatment of the plume source as a Gaussian-shaped thermal anomaly follows previous plume modeling studies such as *Ribe et al.* [1995], *Ribe* [1996], *Ito et al.* [1996, 1999], and *Albers and Christensen* [2001]. For many plumes, knowledge of the detailed structure of the conduit is limited because of seismic resolution constraints. However, *Ito et al.* [1999] calculated the seismic velocity anomalies predicted by an Iceland plume-ridge interaction model that used a Gaussian-shaped thermal source, and they showed that the size of the plume conduit throughout the mantle is similar in dimension to that inferred from a tomography study [*Wolfe et al.*, 1997].

The spatial variation of assigned temperature at the plume source depth is calculated from

$$T_b = T_h + \Delta T \cdot \exp \left\{ - \left[(x - x_o)^2 + (y - y_o)^2 \right] / (d/2.35)^2 \right\} \quad (9)$$

where T_b is the temperature distribution at the bottom boundary, x and y are model Cartesian coordinates, x_o and y_o are the coordinates of the center of the thermal anomaly, d is the diameter of the anomaly, and ΔT is the maximum excess temperature relative to the ambient temperature T_h (Figure 1b). In all models, ΔT is 180°C. Following *Albers and Christensen* [2001], the plume diameter is defined to be the full width at the quarter maxima of the Gaussian-shaped thermal anomaly, and the limits of the plume material are delineated by an isosurface with temperature $(\Delta T/4) + T_h$. The numerical parameter 2.35 in equation (9) derives from the relationship between the full width at half maximum for a Gaussian function and the standard deviation of the Gaussian. In the suite of models, the plume diameter is assigned to be either 125 km or 165 km. It is important to note that the plume is not a point source. The plume is introduced as a continuous temperature field on the bottom boundary of the model domain. Highest temperature values are in the center, and they decay with radial distance to approach ambient mantle temperature. As such, the imposed plume thermal anomaly source spans many grid nodes.

Similar to studies such as *Ito et al.* [1997, 1999] and *Albers and Christensen* [2001], viscosity is calculated according to the Arrhenius formula, with an exponential dependence on temperature and pressure:

$$\eta = A\eta_o \cdot \exp \left\{ [E + \rho_o g(h - z)V]/(RT) - [E + \rho_o gh(V/2)]/(RT_h) \right\} \quad (10)$$

where E is activation energy, V is activation volume, R is the ideal gas constant, η_o is minimum ambient mantle viscosity determined at the half depth of the fluid layer thickness, and A is a parameter controlling the importance of dehydration. For the purposes of numerical stability, maximum and minimum cutoff viscosities are established. The maximum cutoff value is sufficiently high for the formation of a rigid lithosphere layer at the top of the model domain. This study uses two values for minimum cutoff viscosity, 1.5×10^{19} Pa s and 5×10^{18} Pa s. The higher value for minimum cutoff viscosity was used as the base case in a flow pattern study because it eliminates active flow of the plume material due to viscosity contrasts and leaves only the thermal buoyancy contribution. The lower value of minimum viscosity cutoff allows for plume material viscosity to be lower than that of the ambient mantle. Also, the viscosity limits used in this study are controlled by the size of the numerical domain, which is in turn dependent on the amount of random-access memory available. Bigger viscosity contrasts between the plume and the ambient mantle could produce larger waist widths that would exceed the size of domain and therefore could not be modeled.

The pre-exponential parameter A is introduced to allow a subset of model cases to include the effect of dehydration during mantle melting. As the mantle rises and crosses the dry solidus, it may experience an increase in viscosity by a factor of approximately 10–100 due to melting-related dehydration [*Hirth and Kohlstedt*, 1996; *Braun et al.*, 2000]. *Ito et al.* [1999] showed that the incorporation of dehydration produced a high-viscosity layer across mantle depths shallower than the onset of melting, suppressing the effects of the plume's thermal buoyancy within the melting zone. Compared to the case without dehydration, upwelling rates in the melting zone were slower, resulting in lower melt production and thinner crust. The addition of dehydration rheology also promoted lateral spreading of plume material at depths beneath the dry solidus. In a study exploring the dynamics of an off-ridge mantle plume, *Hall and Kincaid* [2003] used a similar

Table 3. Model Cases

Model	d (km)	η_{\min} (Pa s)	θ (deg)	r (km)	A
1	125	1.5×10^{19}	90	50	1
2	165	1.5×10^{19}	90	50	1
3	125	1.5×10^{19}	135	50	1
4	165	1.5×10^{19}	135	50	1
5	125	1.5×10^{19}	180	50	1
6	165	1.5×10^{19}	180	50	1
7	125	1.5×10^{19}	225	50	1
8	165	1.5×10^{19}	225	50	1
9	125	1.5×10^{19}	270	50	1
10	165	1.5×10^{19}	270	50	1
11	125	1.5×10^{19}	315	50	1
12	165	1.5×10^{19}	315	50	1
13	125	1.5×10^{19}	90	75	1
14	165	1.5×10^{19}	90	75	1
15	125	1.5×10^{19}	135	75	1
16	165	1.5×10^{19}	135	75	1
17	125	1.5×10^{19}	180	75	1
18	165	1.5×10^{19}	180	75	1
19	125	1.5×10^{19}	225	75	1
20	165	1.5×10^{19}	225	75	1
21	125	1.5×10^{19}	270	75	1
22	165	1.5×10^{19}	270	75	1
23	125	1.5×10^{19}	315	75	1
24	165	1.5×10^{19}	315	75	1
25	125	1.5×10^{19}	90	100	1
26	165	1.5×10^{19}	90	100	1
27	125	1.5×10^{19}	135	100	1
28	165	1.5×10^{19}	135	100	1
29	125	1.5×10^{19}	180	100	1
30	165	1.5×10^{19}	180	100	1
31	125	1.5×10^{19}	225	100	1
32	165	1.5×10^{19}	225	100	1
33	125	1.5×10^{19}	270	100	1
34	165	1.5×10^{19}	270	100	1
35	125	1.5×10^{19}	315	100	1
36	165	1.5×10^{19}	315	100	1
37	125	1.5×10^{19}	90	50	[1, 50]
38	165	1.5×10^{19}	90	50	[1, 50]
39	125	1.5×10^{19}	135	50	[1, 50]
40	165	1.5×10^{19}	135	50	[1, 50]
41	125	1.5×10^{19}	180	50	[1, 50]
42	165	1.5×10^{19}	180	50	[1, 50]
43	125	1.5×10^{19}	225	50	[1, 50]
44	165	1.5×10^{19}	225	50	[1, 50]
45	125	1.5×10^{19}	270	50	[1, 50]
46	165	1.5×10^{19}	270	50	[1, 50]
47	125	1.5×10^{19}	315	50	[1, 50]
48	165	1.5×10^{19}	315	50	[1, 50]
49	125	1.5×10^{19}	90	75	[1, 50]
50	165	1.5×10^{19}	90	75	[1, 50]
51	125	1.5×10^{19}	135	75	[1, 50]
52	165	1.5×10^{19}	135	75	[1, 50]
53	125	1.5×10^{19}	180	75	[1, 50]
54	165	1.5×10^{19}	180	75	[1, 50]
55	125	1.5×10^{19}	225	75	[1, 50]
56	165	1.5×10^{19}	225	75	[1, 50]
57	125	1.5×10^{19}	270	75	[1, 50]
58	165	1.5×10^{19}	270	75	[1, 50]
59	125	1.5×10^{19}	315	75	[1, 50]
60	165	1.5×10^{19}	315	75	[1, 50]
61	125	1.5×10^{19}	90	100	[1, 50]

treatment of dehydration. They concluded that because of the development of what they termed a high-viscosity “plug” in the uppermost mantle, a significant portion of plume material travels toward the ridge axis at depths below the plume solidus, rather than at shallower depths closer to the lithosphere-asthenosphere boundary. Also, they noted that the effect of the lithosphere-asthenosphere boundary in guiding plume material to the ridge axis is more significant for the case without dehydration.

Several studies have addressed or evaluated the degree to which dehydration rheology may be important in mantle convection and plume-ridge interaction [e.g., Xue and Allen, 2005; Marquart et al., 2007; Delorey et al., 2007; Leroy et al., 2010; Rabinowicz et al., 2012; Howell et al., 2014; Ito et al., 2015]. This investigation models both cases without dehydration rheology (i.e., $A = 1$; Table 2) and cases with dehydration rheology (i.e., $A = [1, 50]$; Table 2). For the latter, A is set to be 1 when temperature of the mantle is beneath the dry solidus and 50 when it is above. To avoid infinite gradients in viscosity, the dehydration parameter is a step function with adjustable smoothing interval. Here the smoothing interval for dehydration is set to be 5°C, defining the abruptness of the transition.

A series of models was run according to the parameters specified in Table 3. In addition to varying the plume diameter and dehydration parameter, as discussed above, models also changed the radial distance of the plume from the triple junction (r) and the azimuth of the plume relative to R_1 (θ). Assigned values for r were 50 km, 75 km, and 100 km; models were also run with the plume directly under the triple junction. For θ , the plume was placed at 90°, 135°, 180°, 225°, 270°, and 315°, roughly spanning the locations of the Azores plume conduit suggested by various studies (summarized in Shorttle et al. [2010]).

Table 3. (continued)

Model	<i>d</i> (km)	η_{\min} (Pa s)	θ (deg)	<i>r</i> (km)	<i>A</i>
62	165	1.5×10^{19}	90	100	[1, 50]
63	125	1.5×10^{19}	135	100	[1, 50]
64	165	1.5×10^{19}	135	100	[1, 50]
65	125	1.5×10^{19}	180	100	[1, 50]
66	165	1.5×10^{19}	180	100	[1, 50]
67	125	1.5×10^{19}	225	100	[1, 50]
68	165	1.5×10^{19}	225	100	[1, 50]
69	125	1.5×10^{19}	270	100	[1, 50]
70	165	1.5×10^{19}	270	100	[1, 50]
71	125	1.5×10^{19}	315	100	[1, 50]
72	165	1.5×10^{19}	315	100	[1, 50]
73	125	5×10^{18}	90	50	1
74	165	5×10^{18}	90	50	1
75	125	5×10^{18}	135	50	1
76	165	5×10^{18}	135	50	1
77	125	5×10^{18}	180	50	1
78	165	5×10^{18}	180	50	1
79	125	5×10^{18}	225	50	1
80	165	5×10^{18}	225	50	1
81	125	5×10^{18}	270	50	1
82	165	5×10^{18}	270	50	1
83	125	5×10^{18}	315	50	1
84	165	5×10^{18}	315	50	1
85	125	5×10^{18}	90	75	1
86	165	5×10^{18}	90	75	1
87	125	5×10^{18}	135	75	1
88	165	5×10^{18}	135	75	1
89	125	5×10^{18}	180	75	1
90	165	5×10^{18}	180	75	1
91	125	5×10^{18}	225	75	1
92	165	5×10^{18}	225	75	1
93	125	5×10^{18}	270	75	1
94	165	5×10^{18}	270	75	1
95	125	5×10^{18}	315	75	1
96	165	5×10^{18}	315	75	1
97	125	5×10^{18}	90	100	1
98	165	5×10^{18}	90	100	1
99	125	5×10^{18}	135	100	1
100	165	5×10^{18}	135	100	1
101	125	5×10^{18}	180	100	1
102	165	5×10^{18}	180	100	1
103	125	5×10^{18}	225	100	1
104	165	5×10^{18}	225	100	1
105	125	5×10^{18}	270	100	1
106	165	5×10^{18}	270	100	1
107	125	5×10^{18}	315	100	1
108	165	5×10^{18}	315	100	1
109	125	5×10^{18}	90	50	[1, 50]
110	165	5×10^{18}	90	50	[1, 50]
111	125	5×10^{18}	135	50	[1, 50]
112	165	5×10^{18}	135	50	[1, 50]
113	125	5×10^{18}	180	50	[1, 50]
114	165	5×10^{18}	180	50	[1, 50]
115	125	5×10^{18}	225	50	[1, 50]
116	165	5×10^{18}	225	50	[1, 50]
117	125	5×10^{18}	270	50	[1, 50]
118	165	5×10^{18}	270	50	[1, 50]
119	125	5×10^{18}	315	50	[1, 50]
120	165	5×10^{18}	315	50	[1, 50]
121	125	5×10^{18}	90	75	[1, 50]
122	165	5×10^{18}	90	75	[1, 50]

2.4. Model Results Postprocessing

For postprocessing, calculated temperature, velocity field, and viscosity were extracted by evaluating solutions on a uniformly spaced grid with $\Delta x = \Delta y = 12.5$ km and $\Delta z = 5$ km for each model. Plume waist width *W* was determined along each of *R*₁, *R*₂, and *R*₃ using a temperature isosurface. Plume volume flux was calculated following studies such as *Albers and Christensen* [2001] by evaluating the two-dimensional integral

$$Q = \Delta T^{-1} \iint w(T - T_h) dx dy \quad (11)$$

on the bottom boundary. It is important to note that this volume flux is based on properties of the plume at its source depth. There are several different definitions in the literature associated with the term “volume flux.” The one that is used in this study is not equivalent to the volume flux derived from the swell’s morphology, volcanic volume flux, or magmatic volume flux [e.g., *Vidal and Bonneville*, 2004; *Van Ark and Lin*, 2004]. Depending on the model case, plume volume fluxes ranged from 5.2 m³/s to 28 m³/s.

Buoyancy flux is defined as

$$B = Q\rho_o\alpha(\Delta T) \quad (12)$$

following studies such as *Ribe et al.* [1995] and *Albers and Christensen* [2001]. Volume fluxes of $Q = 5.2$ – 28 m³/s correspond to buoyancy fluxes of $B = 0.09$ – 0.5 Mg/s. Several investigations have quantified plume buoyancy fluxes using the shape of the associated bathymetric swells. The buoyancy fluxes calculated here overlap the range of $B = 0.38$ – 0.85 Mg/s determined for the Azores in *King and Adam* [2014], and they are lower than the Azores flux of $B = 1.1$ Mg/s in *Sleep* [1990]. It is worthwhile to note that *King and Adam* [2014] discuss reasons why their buoyancy fluxes differ from those of *Sleep* [1990]. They also suggest that their uncertainties may be as much as 50–80% for hot spots with relatively small swells.

Table 3. (continued)

Model	d (km)	η_{\min} (Pa s)	θ (deg)	r (km)	A
123	125	5×10^{18}	135	75	[1, 50]
124	165	5×10^{18}	135	75	[1, 50]
125	125	5×10^{18}	180	75	[1, 50]
126	165	5×10^{18}	180	75	[1, 50]
127	125	5×10^{18}	225	75	[1, 50]
128	165	5×10^{18}	225	75	[1, 50]
129	125	5×10^{18}	270	75	[1, 50]
130	165	5×10^{18}	270	75	[1, 50]
131	125	5×10^{18}	315	75	[1, 50]
132	165	5×10^{18}	315	75	[1, 50]
133	125	5×10^{18}	90	100	[1, 50]
134	165	5×10^{18}	90	100	[1, 50]
135	125	5×10^{18}	135	100	[1, 50]
136	165	5×10^{18}	135	100	[1, 50]
137	125	5×10^{18}	180	100	[1, 50]
138	165	5×10^{18}	180	100	[1, 50]
139	125	5×10^{18}	225	100	[1, 50]
140	165	5×10^{18}	225	100	[1, 50]
141	125	5×10^{18}	270	100	[1, 50]
142	165	5×10^{18}	270	100	[1, 50]
143	125	5×10^{18}	315	100	[1, 50]
144	165	5×10^{18}	315	100	[1, 50]

Seafloor topography variations were determined using two methods, because the origin of hot spot swells is still under debate. One method calculated dynamic topography and the other method calculated thermal (or isostatic) topography. In this study, isostatic topography is generated by variations in the subsurface thermal structure, which result in density anomalies and seafloor depth variations. For dynamic topography, the dynamics of the system are important: the plume and ridge upwelling velocities are the main factors controlling bathymetry variations.

We compute dynamic topography following studies such as *Adam et al.* [2013]. The normal stress shaping the topography of the top surface of the model domain is

$$\sigma_{rr} = -p + 2\eta(dw/dz) \quad (13)$$

Dynamic topography is then calculated to be

$$\Delta h_d = \sigma_{rr} / [(\rho_o - \rho_w) * g] \quad (14)$$

To emphasize the effect of the plume, we present dynamic topography variations by removing a constant value equal to the depth along the $R_1 - R_2$ ridge axis far away from the plume source. In other words, dynamic topography variations outside the plume-affected area are set to 0 km.

For this study, we define thermal (or isostatic) topography to depend on mantle density variations due to temperature structure according to equation (15) below. Even in the absence of a plume, variations in thermal structure beneath an RRR triple junction may result in areas of shallower and deeper seafloor, as shown in *Georgen* [2008] and *Georgen and Sankar* [2010]. For this study, in order to isolate the contribution of the mantle plume to variations in topography, it was necessary to calculate additional models without the plume thermal anomaly. Specifically, four cases were run, using both of the defined viscosity ranges and both a dehydrating ($A = [1, 50]$) and a nondehydrating ($A = 1$) mantle. In these four ridge-only models, all calculated topography is due only to horizontal and vertical variations in triple junction temperature pattern, not to the presence of a mantle plume. For each of the temperature solutions calculated in Table 3, the temperature solution for the corresponding ridge-only case was subtracted. For example, for case 126, the corresponding ridge-only model had η_{\min} set to 5×10^{18} Pa s and a dehydrating mantle. Following earlier studies such as *Albers and Christensen* [2001], *Georgen and Lin* [2002], *Georgen* [2008], *Georgen and Sankar* [2010], and *Georgen* [2011], topographic variations were determined using

$$\Delta h_t = [a\rho_o / (\rho_c - \rho_w)] \int (T - T_o) dz \quad (15)$$

where T_o is temperature of the model without the thermal anomaly. It was assumed that vertical mantle columns are in isostatic equilibrium at a depth of 200 km.

Melt fraction, melt production rate, and crustal thickness were calculated in a postprocessing step with temperature and velocity solutions from the series of models. The melting model used is similar to that of *Reid and Jackson* [1981], *McKenzie and Bickle* [1988], and *Sparks and Parmentier* [1993] as followed by *Georgen and Sankar* [2010], with the solidus defined as

$$T_{\text{solidus}} = 1160[^\circ\text{C}] + 3.25z \quad (16)$$

where z is depth in kilometers. Melt fraction F is

$$F = (T - T_{\text{solidus}})/350[^\circ\text{C}] \quad (17)$$

and melt production rate Γ is

$$\Gamma = \nabla F \cdot \mathbf{u} \quad (18)$$

To predict crustal thickness variations, it is assumed that melt migrates vertically and all of the melt reaches a ridge axis. Additionally, it is also assumed that the mantle and the plume are homogenous, compositionally indistinguishable material with no heat exchange between melt and surrounding mantle. Following *Braun et al.* [2000], the melt fraction is limited to 18% as this value is assumed to be the amount of melt that is produced before the exhaustion of clinopyroxene. Integrating the melt production rate over the domain depth (z) yields the distribution of the vertical cumulative melt production in the horizontal (x - y) plane. The depth at which integration starts is limited to 96 km to prevent unrealistic crustal thickness in the region of the plume conduit. At a given (x , y) point, melt is allocated to a specific spreading ridge domain based upon the ratio of the half-spreading rates of the nearest two ridge branches. Finally, for a given ridge, crustal thickness is determined by integrating the cumulative melt production rate along lines perpendicular to that ridge and within the ridge's melt allocation domain, and dividing by the ridge full spreading rate. This simplified model of melting and melt pooling gives first-order, relative crustal thickness variations along the ridges. Future modeling can systematically explore the effects of using other criteria for allocating melt to a particular ridge axis (e.g., lithospheric slope).

2.5. Model Limitations and Future Modeling

This investigation systematically investigates the general fluid dynamics of plume–triple junction interactions using a suite of numerical models and an idealized, representative triple junction geometry. Future studies may expand upon this work by including additional characteristics that are specific to a plume–triple junction system of interest. These factors could include time dependence, ridge migration, and ridge segmentation. Time-dependent [e.g., *Howell et al.*, 2014] versus stationary solutions of numerical models would permit simulation of a pulsing plume (i.e., time-dependent volumetric plume flux). Incorporation of ridge segmentation patterns [*Georgen*, 2014] would move modeling from generalized triple junction geometry to individual geological settings. As the lithospheric plates are in constant motion with respect to a given underlying mantle plume, the addition of ridge migration and ridge jumps [e.g., *Mittelstaedt et al.*, 2012] would produce a more realistic dynamical model. Finally, this study, like that of *Albers and Christensen* [2001], emphasizes fluid dynamics. Subsequent studies can combine geodynamical calculations with petrological melting models. Melting can be incorporated into the conservation equations, and the buoyancy force can include contributions from melt retention and melt depletion.

3. Model Results and Discussion

3.1. Temperature and Velocity Fields

Here the dispersion of the plume material in the vicinity of the triple junction will be introduced using a few characteristic models. Figure 3 (left column) presents results from Model 1 (Table 3), which is arbitrarily defined as the base case for model comparison. The plume conduit is located along R_3 ($\theta = 90^\circ$). Ascending plume material is channeled along the R_3 axis resulting in elevated temperatures to ~ 250 km “east” of the triple junction. A portion of the plume material also reaches the $R_1 - R_2$ ridge axis, and it is asymmetrically diverted to the “south.” Plume dispersion along R_2 is enhanced by the along-axis components of surface plate divergence that are in the same direction. The relatively smaller distance the plume material disperses along R_1 toward the “north” can be attributed to the southward-directed component of surface plate velocity to the “west” of the triple junction. Only a small amount of plume material crosses the $R_1 - R_2$ axis.

Compared to Model 1, Model 2 increases the volume flux of the plume conduit by increasing the plume radius (from $d = 125$ km to $d = 165$ km) (Table 3). Figure 3 (middle column) shows that the general trends in the flow patterns in Model 1 are preserved. The overall shape of the plume dispersion in Model 2 is roughly the same as the results from Model 1, although the plume extends over a larger area.

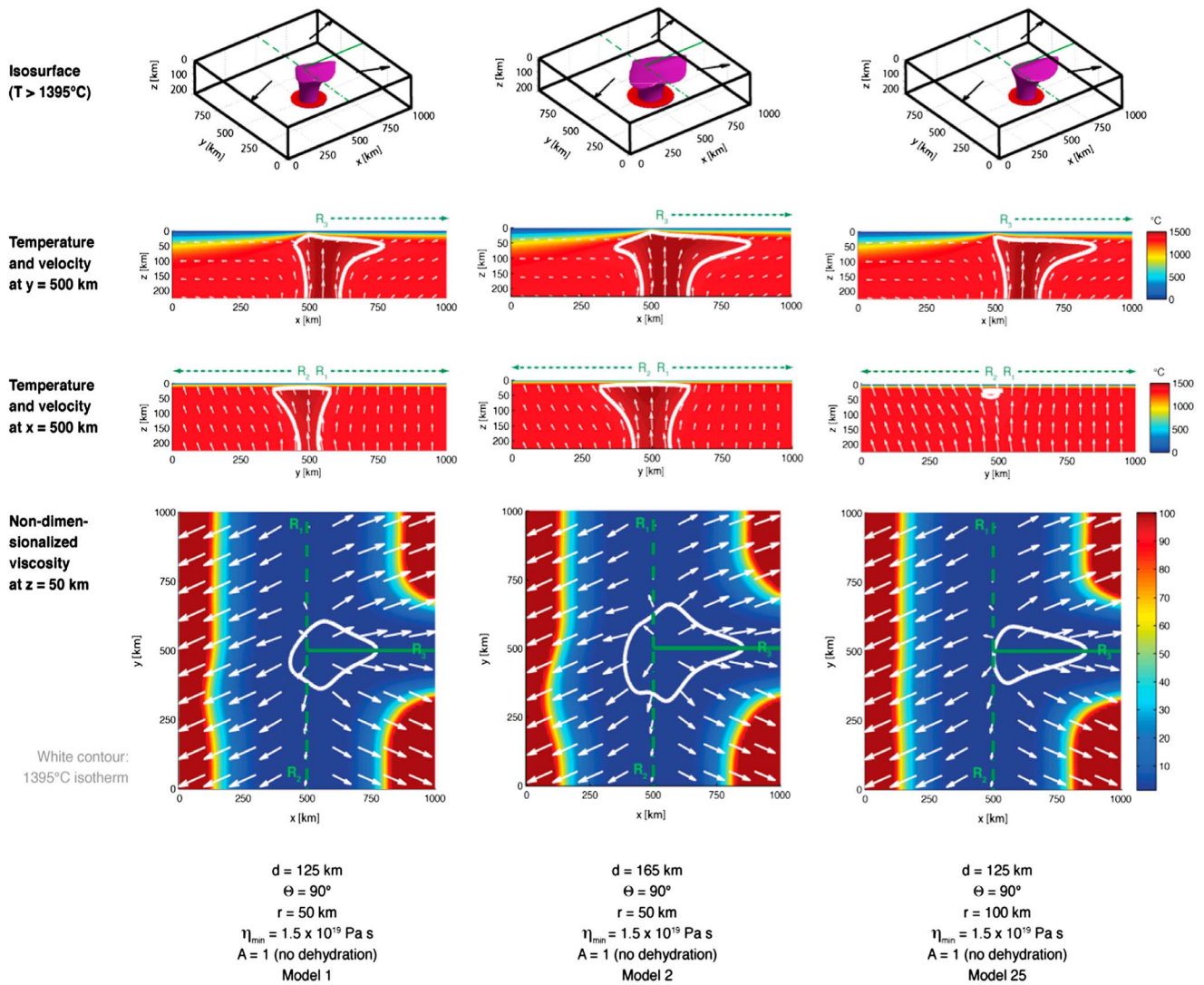


Figure 3. (left column) Results from Model 1 (Table 3). Top panel shows numerical domain with plume dispersion pattern. Top surface plate vectors are shown with black arrows and red circle on bottom boundary indicates area with temperature greater than 1350°C ; lower values are white. Purple isosurface encapsulates the volume of the model domain for which calculated temperatures are greater than or equal to 1395°C . An artificial illumination has been applied to the isosurface to emphasize its shape. Green dashed, dash-dotted, and solid lines indicate R_1 , R_2 , and R_3 , respectively. Second panel in left column shows calculated temperature and velocity solutions extracted along a vertical plane at $y = 500 \text{ km}$. Distances greater than $x = 500 \text{ km}$ correspond to R_3 . Third panel is similar to second panel, but extracted along a vertical plane at $x = 500 \text{ km}$ (i.e., the $R_1 - R_2$ axis). Bottom panel presents a horizontal slice through the model domain, extracted at 50 km below the top surface, showing calculated velocity and viscosity solutions. Nondimensionalized viscosity scale is described in the text. (middle column) Same as Figure 3 (left column) but for Model 2. (right column) Same as Figure 3 (left column) but for Model 25.

Moving the origin of the plume conduit by 50 km eastward along the axis of R_3 (Model 25, Figure 3, right column), compared to the base case, almost completely prevents plume material from crossing the $R_1 - R_2$ axis. Model 25 does not incorporate dehydration viscosity. If the dehydration parameter, as discussed earlier in the text, is allowed to assume values $A = [1, 50]$ depending on the difference between mantle temperature and solidus temperature, the effects can be seen in Figure 4 (left column). A comparison of models 25 and 61 shows how, when dehydration viscosity is incorporated, the lateral flow of the plume material is suppressed by off-axis areas with high viscosity. Plume material does not follow the lithosphere-asthenosphere boundary in Model 61 as compared to Model 25, and plume material does not intersect the $R_1 - R_2$ axis.

Model 6 repositions the plume conduit along the axis of R_2 ($\theta = 180^{\circ}$), at a distance of $r = 50 \text{ km}$ from the triple junction (Figure 4, middle column). As might be anticipated, plume material flows a longer distance south

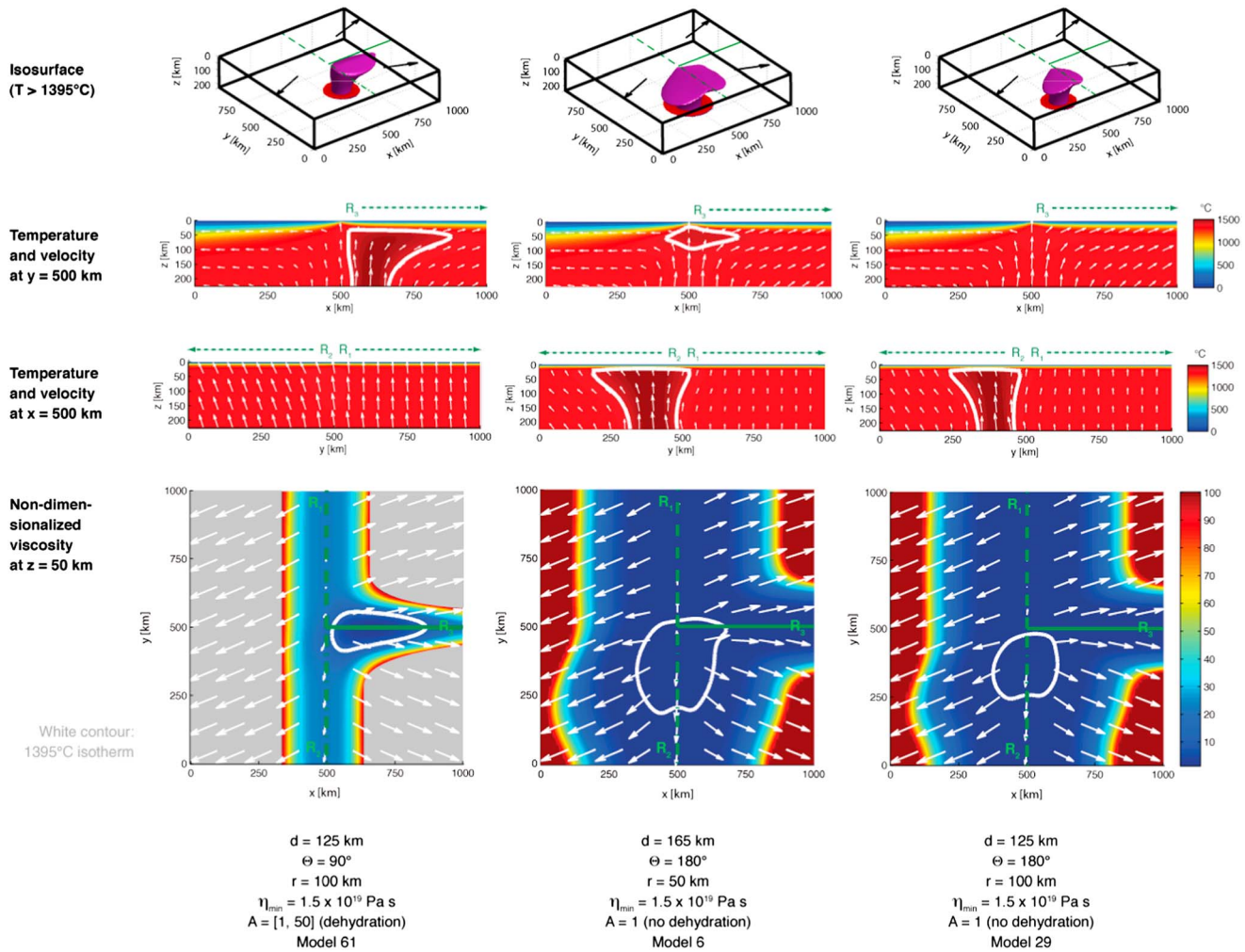


Figure 4. (left column) As for Figure 3 but for Model 61. Gray shading in the bottom panel is used to block off-axis areas with relatively high normalized viscosity, where some variability occurs due to the implementation of the dehydration function. This variability does not affect the dynamics of plume dispersion described in the text. (middle column) Results for Model 6. (right column) Results for Model 29.

along R_2 than in Model 1 (Figure 3). Plume material reaches $\sim 240 \text{ km}$ away from the triple junction along R_3 , and it extends $\sim 160 \text{ km}$ to the west of the $R_1 - R_2$ axis. Setting a plume with a relatively small flux 100 km south of the triple junction along the R_2 axis (Model 29; Figure 4, right column) results in a total absence of plume material both to the north of the triple junction and along R_3 . However, increasing the volume flux for a plume in the same location (Model 30; Figure 5, left column) causes a portion of the plume material to cross the R_3 axis at shallow depths.

All the results discussed so far were for the case of no viscosity contrast between plume material and the ambient mantle. Reducing the minimum cutoff viscosity to $\eta = 5 \times 10^{18} \text{ Pa s}$ allows the plume material to have lower viscosity than the ambient mantle. As a result, plume dispersion generally occurs over a larger region. This can be seen by comparing Model 1 (Figure 3) to Model 73 (Figure 5). An additional sample calculation using a minimum cutoff viscosity of $\eta = 5 \times 10^{18} \text{ Pa s}$ is shown in Figure 5 (right column).

3.2. Mantle Plume Contribution to Seafloor Topography

The contribution of the mantle plume to the thermal (isostatic) axial topography for each model from Table 3 is calculated as described above. As suggested by equation (15), variations in thermal topography profiles are directly proportional to the thickness of the mantle plume material underneath a given point along a ridge axis. It is important to note that this study reports the full values of the isostatic topography due to mantle

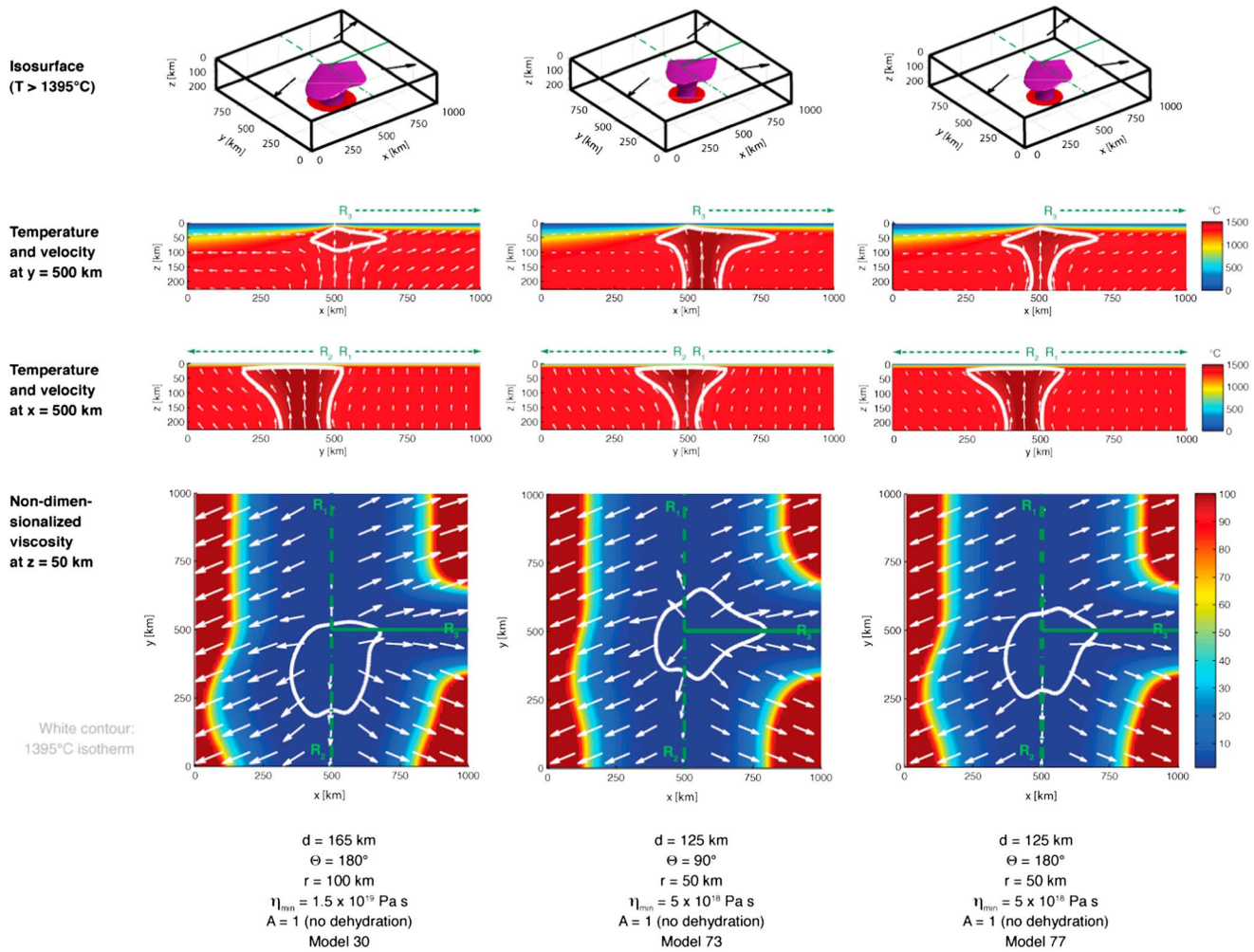


Figure 5. (left column) As for Figure 3 but for Model 30. (middle column) Results for Model 73. (right column) Results for Model 77.

temperature variations. Investigations of mantle Bouguer anomaly for plume-affected sections of ridge along the Reykjanes Ridge [Ito et al., 1996] and Galapagos Spreading Center [Canales et al., 2002] suggest that mantle thermal variations contribute roughly 25–30% to the observed topography, with the remainder of the seafloor variation attributed to crustal sources. Accordingly, investigations such as Georgen [2008] and Georgen and Sankar [2010] applied this percentage to their total values of calculated isostatic topography when reporting predicted bathymetry variation. To allow for different percentages of the partitioning of the topography between crustal and mantle sources, the present study does not perform this step.

Figure 6 shows the thermal topography for a subset of models with the plume conduit located at $r = 100 \text{ km}$ from the triple junction and with the minimum viscosity cutoff limit $5 \times 10^{18} \text{ Pa s}$, for all values of the azimuth (θ) and for runs both with (b and d) and without (a and c) dehydration. (The rest of the models show similar trends in thermal topography and therefore will not be presented here.) The maximum value of the thermal topography variation along the ridges is $\sim 2 \text{ km}$ (Figure 6), and it occurs when the plume conduit is ridge centered (i.e., $\theta = 90^\circ$ (Figures 6a and 6b) or 180° (Figures 6c and 6d)). The least pronounced variations in along-axis thermal topography for a given ridge axis generally occur when a plume is located farther away from that ridge. For example, Figure 6b shows that for the case with dehydration, the lowest thermal topography along R_3 ($x > 500 \text{ km}$) occurs with a weaker plume (smaller plume diameter) located along R_2 ($\theta = 180^\circ$). In this case, the topographic variation is only $\sim 0.2 \text{ km}$. In general, the addition of dehydration rheology results in topographic peaks of lower amplitude and shorter along-axis length. For example, for $\theta = 90^\circ$, Figure 6a without dehydration rheology shows a peak of about $\sim 0.1 \text{ km}$ higher than Figure 6b with

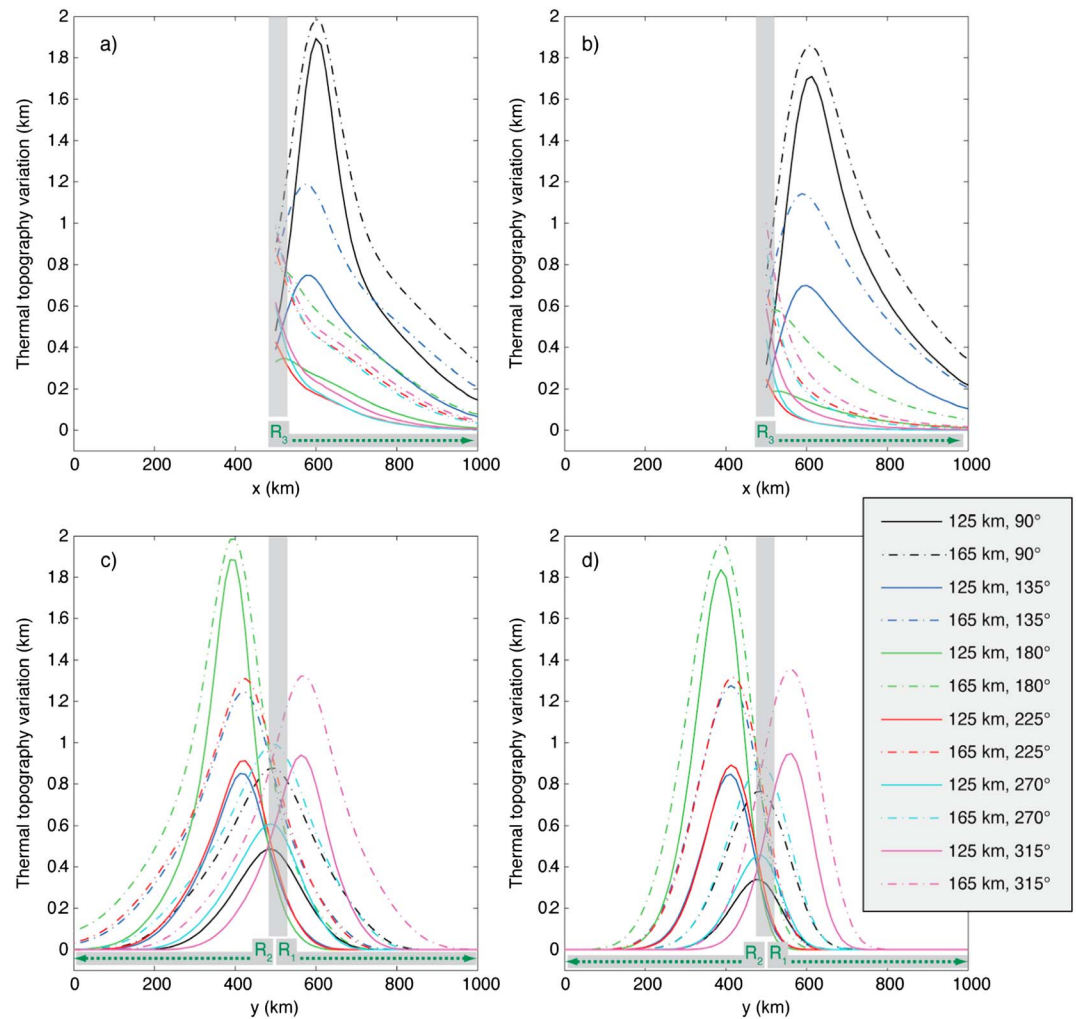


Figure 6. Thermal (or isostatic) topography variations for all models with $r = 100$ km and $\eta_{\min} = 5 \times 10^{18}$ Pa s. Azimuth (θ) and plume diameter (d) are indicated by a common legend in Figure 6d. (a) Calculated topographic variations along $y = 500$ km. Distances greater than $x = 500$ km correspond to R_3 . These models do not incorporate dehydration viscosity ($A = 1$). (b) Same as Figure 6a but with dehydration viscosity ($A = [1, 50]$). (c) Calculated topographic variations along $x = 500$ km (i.e., the $R_1 - R_2$ axis). $A = 1$. (d) Same as Figure 6c but with $A = [1, 50]$.

dehydration. For the case of $\theta = 315^\circ$, the plume-related topographic anomaly along R_1 is ~ 200 km shorter when dehydration mantle rheology is used (Figure 6c compared to Figure 6d).

The results of selected dynamic topography calculations are shown in Figure 7. For all runs depicted in Figure 7, $r = 100$ km, $A = 1$ (i.e., dehydration viscosity is not implemented), and minimum viscosity is 5×10^{18} Pa s. For $\theta = 90^\circ$ and $\theta = 270^\circ$, the depth anomaly maximum along $R_1 - R_2$ is centered on the triple junction (Figures 7a and 7i). It is shifted to the south of the triple junction for $\theta = 135^\circ$, 180° , and 225° by roughly 100 km (Figures 7c, 7e, and 7g). For $\theta = 315^\circ$, the peak is approximately 50–100 km to the north of the triple junction (Figure 7k). In these plots, the maximum amplitude of dynamic topography variation along $R_1 - R_2$, roughly 2 km, is calculated for $\theta = 180^\circ$ and $d = 165$ km. Focusing on R_3 , dynamic topography variation is less than 1 km for plume azimuths greater than or equal to 180° (Figures 7f, 7h, 7j, and 7l). For $\theta = 90^\circ$ and $d = 165$ km, the variation is greater than 1 km (Figure 7b), while for $\theta = 135^\circ$ and $d = 165$ km, it is approximately 1 km (Figure 7d). The location of the peak for $\theta = 90^\circ$ is approximately 60–75 km east of the triple junction (Figure 7b).

It is possible to make several observations about isostatic and dynamic topography by comparing Figures 6a and 6c to Figure 7. For all of the model runs in those figures, $r = 100$ km, $A = 1$ (i.e., dehydration viscosity was

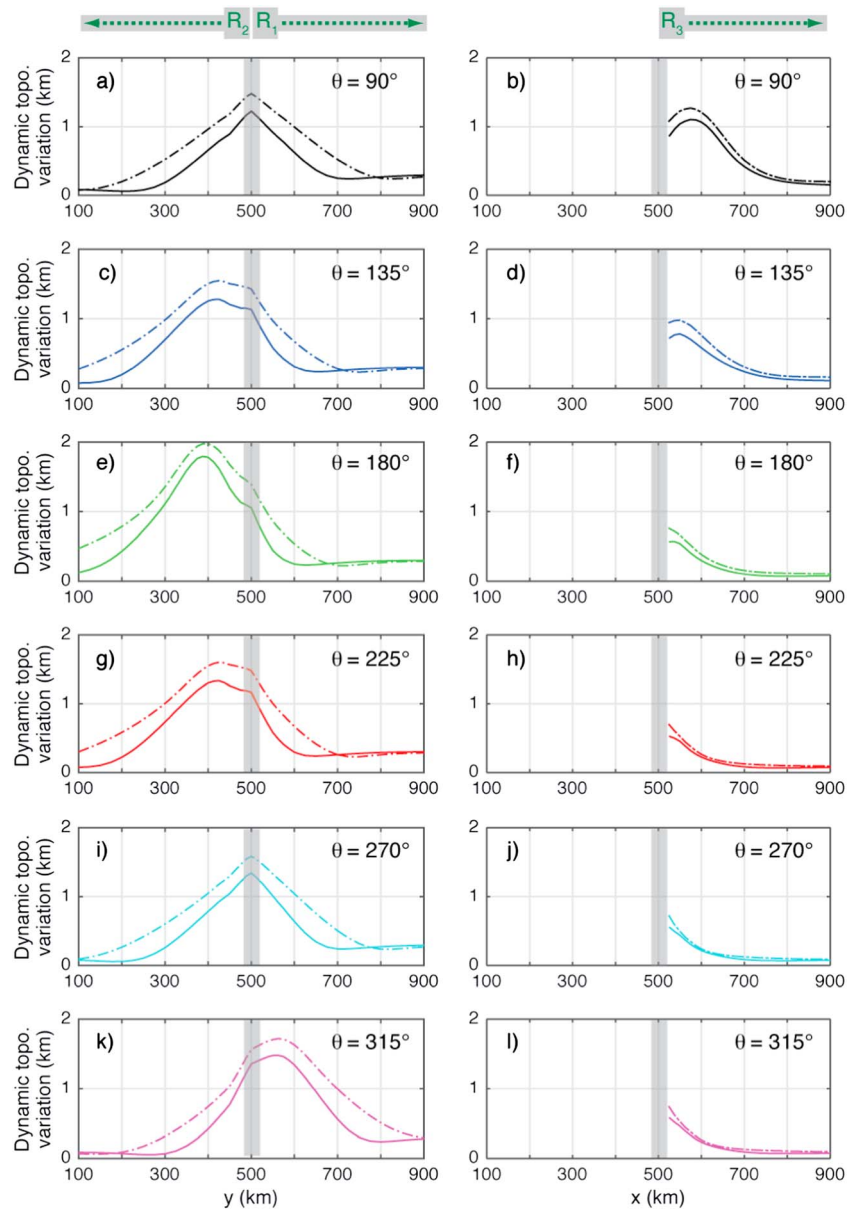


Figure 7. Dynamic topography calculations for models with $r = 100$ km, $A = 1$ (i.e., dehydration viscosity is not implemented), and a minimum viscosity of 5×10^{18} Pa s. As in Figure 6, dashed lines show results for model runs with $d = 165$ km, and solid lines indicate $d = 125$ km. (a, c, e, g, i, and k) Results for the $R_1 - R_2$ axis. (b, d, f, h, j, and l) Topography variations along the R_3 axis. Plume azimuth (θ) is indicated in the upper right portion of each panel.

not implemented), and minimum viscosity was 5×10^{18} Pa s. In light of the discussion above regarding the percentage of the total isostatic anomaly attributed to crustal versus mantle sources, and the uncertainty this introduces in comparing the amplitudes of the isostatic and dynamic topography variations, the focus here is on general profile shape, the location of the peak values, and the wavelengths of the along-axis anomalies.

In general, the profiles of dynamic and isostatic topography have similar overall shape, and the peak values are located at approximately the same distance from the triple junction. Along $R_1 - R_2$, similarity also exists in the asymmetry of the topographic variation with respect to the location of the peak value. For example, for $\theta = 180^\circ$ and $d = 125$ km, both the dynamic (Figure 7e) and the isostatic (Figure 6c) topography anomalies extend approximately 200 km to the north and 300 km to the south of the peak value. This similarity is perhaps not surprising, since dynamic and isostatic topography are both sensitive to factors such as the

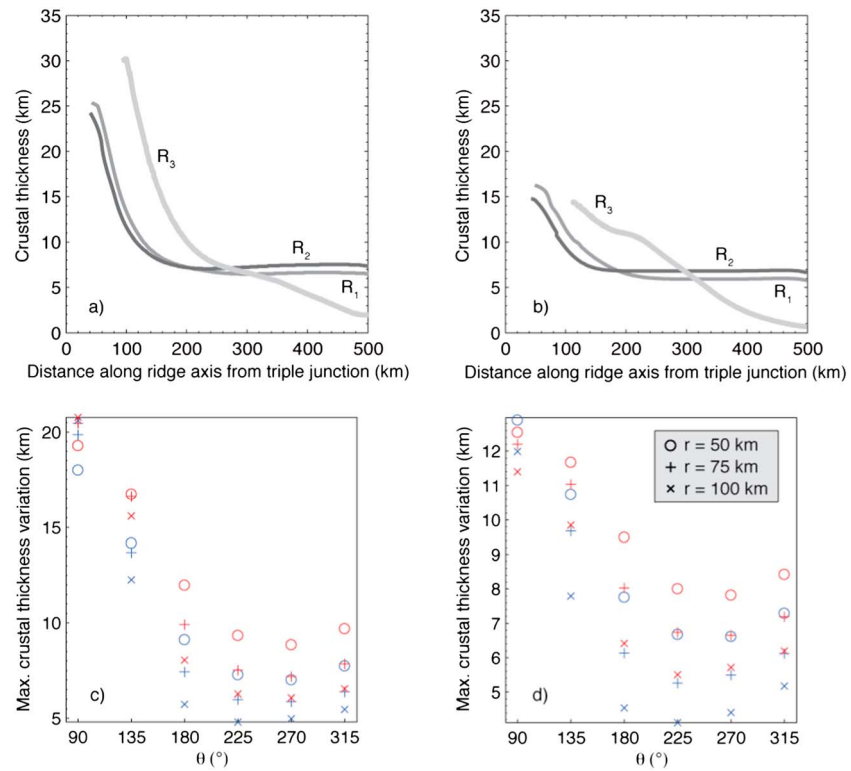


Figure 8. (a and b) Crustal thickness predictions along each ridge axis as a function of distance from triple junction. Figure 8a shows results from Model 73, and Figure 8b shows results from Model 109. These use the same plume conduit location and diameter, but in Figure 8a $A = 1$ and in Figure 8b $A = [1, 50]$. Figures do not plot crustal thicknesses close to the triple junction (less than ~ 40 km for R_1 and R_2 , and less than ~ 100 km for R_3) as these are undervalued because of the method chosen for the melt-ridge allocation. (c and d) Maximum crustal thickness variation along various ridge axes as a function of plume conduit azimuth (θ). Blue and red symbols indicate plume diameters (r) of 125 km and 165 km, respectively. “Circle,” “plus,” and “cross” symbols indicate the distance of the plume from the triple junction (r), according to the common legend in Figure 8d. Figure 8c shows results from models along R_3 with $\eta_{\min} = 1.5 \times 10^{19}$ Pa s and $A = 1$. Figure 8d is the same as in Figure 8c except with $A = [1, 50]$. Note that the y axis extents of Figures 8c and 8d differ.

plume location and plume diameter. With respect to the wavelength of the along-axis anomalies, isostatic topography is generally somewhat greater than dynamic topography. This could be because the dynamic topography is sensitive to the region of focused vertical upwelling in the plume conduit, whereas lateral advection of hot plume material at shallow depths results in broader horizontal distribution of mantle thermal anomalies, to which isostatic topography is sensitive.

3.3. Model Crustal Thickness Calculations

Crustal thickness was calculated for all models in Table 3. In general, predicted crustal thickness decreases along the ridges as a function of distance away from the triple junction and the assigned location of the mantle plume. Two example cases are shown in Figures 8a and 8b. At distances of several hundred kilometers from the triple junction, the predicted crustal thickness for R_3 approaches 0 km, which is qualitatively consistent with observational data from ultraslow-spreading ridges [e.g., Dick et al., 2003]. Along $R_1 - R_2$, crustal thicknesses are approximately 6–8 km at large distances from the triple junction, which is in line with average global oceanic crustal thickness in areas that are not affected by a mantle plume. Closer to the plume, crustal thickness is predicted to be significantly less when dehydration viscosity is used (Figure 8b) compared to when viscosity is dependent only on pressure and temperature (Figure 8a). This result is consistent with prior plume-ridge interaction models that employ dehydration rheology [e.g., Ito et al., 1999]. As noted earlier, when these studies incorporated dehydration in mantle viscosity, upwelling rates in the melting zone decreased compared to models without dehydration, resulting in lower melting rates and thinner crust.

Since the quantity of interest in the suite of calculations is how crustal thickness changes along the ridge axes as a function of model parameters, the maximum crustal thickness variation along all three of the ridges was determined for each model run. For example, in Figure 8a the maximum value of the calculated crustal thickness along R_1 is ~ 26 km and the minimum is ~ 6 km, resulting in ~ 20 km of maximum crustal thickness variation along R_1 for this model case. Figures 8c and 8d provide summary plots of maximum crustal thickness variation along R_3 for a subset of the model runs. In general, plumes with diameters of $d = 165$ km produced greater maximum crustal thickness variations than plumes with diameters of $d = 125$ km, as would be expected. Also, in most cases, maximum crustal thickness variation for a given azimuth was greatest for plumes located closest to the triple junction ($r = 50$ km). For example, for a plume with $d = 125$ km located at $\theta = 180^\circ$ in Figure 8c, moving the plume from $r = 50$ km to $r = 100$ km resulted in a decrease of more than 4 km in calculated maximum crustal thickness variation.

Figure 8c shows trends in the maximum crustal thickness variation along R_3 when $\eta_{\min} = 1.5 \times 10^{19}$ Pa s and $A = 1$. As the plume conduit changes azimuth from $\theta = 90^\circ$ to $\theta = 270^\circ$ the maximum crustal thickness variations span values from ~ 21 km to ~ 5 km. The highest maximum crustal thickness variation (~ 21 km) occurs when the plume conduit is located directly beneath R_3 ($\theta = 90^\circ$), and the smallest maximum crustal thickness variation (~ 5 km) is predicted when $r = 100$ km, $d = 125$ km, and $\theta = 225^\circ$. As noted in the previous paragraph, for most model runs the maximum crustal thickness variation decreases with increasing r . However, for $\theta = 90^\circ$ in Figure 8c, maximum crustal thickness variations for $r = 50$ km are somewhat less than those for $r = 75$ km and $r = 100$ km. This irregularity is due to the method of melt allocation to each ridge axis, which assigns melt to a particular ridge branch depending on the ratio of the spreading rates. Thus, a dispersing plume located close to the triple junction underneath R_3 will have some of its melt assigned to R_1 and R_2 because the slow half-spreading rate of R_3 defines a relatively narrow melt allocation zone. Figure 8d shows results when mantle dehydration is incorporated. The values of maximum crustal thickness variation along R_3 decrease in Figure 8d compared to Figure 8c, spanning a range from ~ 4 km to ~ 13 km.

3.4. Influence of the Triple Junction on Plume Dispersal

One way of exploring the influence of the triple junction on the dispersion of plume material is to compare the suite of models in Table 3 to corresponding cases where the plume is located beneath the triple junction (Figure 9). To accomplish this, the areal dispersion of each plume was calculated at a depth of 50 km (i.e., within the partial melting zone), assuming that the plume is defined by temperatures greater than 1395°C . This area was then normalized to the areal dispersion of a plume with the same properties (i.e., diameter, minimum viscosity, and range of the dehydration parameter A) but located beneath the triple junction.

The normalized area of the non-triple-junction-centered plumes depends on the plume volume flux (which involves plume diameter and excess temperature), the viscosity contrast between the plume and ambient mantle, the azimuth of the plume, and the distance of the plume from the triple junction. Figure 9 shows how normalized area varies as a function of the latter two factors, plume azimuth and the distance of the plume from the triple junction. For all of the cases plotted, $A = 1$. Plume volume flux increases from Figures 9b to 9e (see figure caption for numerical details). With increasing plume flux, two trends can be observed. First, there is a weaker dependence of the normalized area on the azimuth (i.e., a value closer to 1). Second, there is a weaker dependence of the normalized area on the radial distance of the plume conduit. For example, for $\theta = 270^\circ$ and $r = 100$ km, normalized area in Figure 9b is 0.5–0.6. However, in Figure 9e, the corresponding normalized area is 0.8–0.9. As another example, from Figures 9b to 9e for $\theta = 270^\circ$, the difference in normalized area between $r = 100$ km and $r = 50$ km decreases from >0.2 to approximately 0.1.

Figure 9 can be used to show how the presence of R_3 and the third plate affects plume advection patterns. If R_3 were not present and two plates diverged symmetrically from the $R_1 - R_2$ axis, then a plume with given values of r and d should advect in an identical manner regardless of whether $\theta = 270^\circ$ or $\theta = 90^\circ$. In this scenario, plume upslope flow along the thickening lithosphere would occupy the same horizontal area despite whether the plume was located to the west or east of the $R_1 - R_2$ axis. In all cases plotted in Figure 9, the normalized area is >0.9 for $\theta = 90^\circ$, regardless of the value of the parameter r . That is, the area over which the plume spreads is very close to the case where the plume is centered under the triple junction. However, for $\theta = 270^\circ$, normalized area ranges from approximately 0.5 to 1 and it shows stronger sensitivity to the parameter r . In cases where dehydration viscosity is not used, a plume that is located under ultraslow-

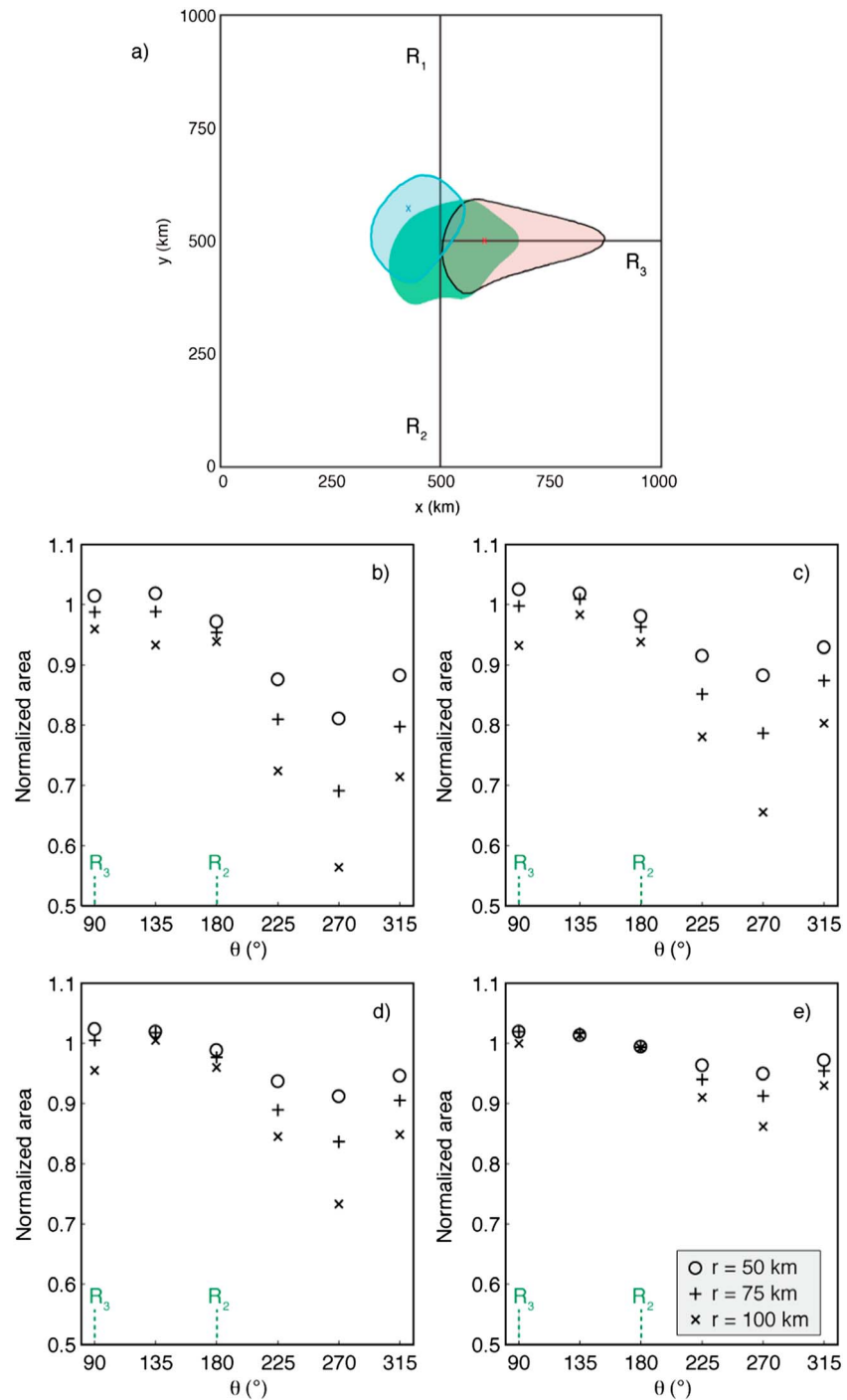


Figure 9. (a) Horizontal slice of the model domain at 50 km depth, showing the areal dispersion of a plume with diameter 125 km for different positions of the plume stem. Green filled shape is the area occupied by plume material (defined as $T > 1395^\circ\text{C}$) when the plume is located beneath the triple junction. Red and blue contours define the areal dispersion of plume material from Models 25 and 35 (Table 3), respectively, with “cross” symbols indicating the location of the plume conduit center on the bottom of the model domain. (b–e) Area of the plume at 50 km depth normalized to the case of the same plume located beneath the triple junction, as a function of the plume azimuth (θ). For all model runs shown, $A = 1$. Different symbols for data points represent different radial distances of the plume conduit from the triple junction (r) as indicated in Figure 9e. Figure 9b plots all runs from Table 3 with $d = 125$ km and $\eta_{\min} = 1.5 \times 10^{19}$ Pa s. Similarly, Figure 9c plots all runs from Table 3 with $d = 165$ km and $\eta_{\min} = 1.5 \times 10^{19}$ Pa s, Figure 9d plots all runs with $d = 125$ km and $\eta_{\min} = 5 \times 10^{18}$ Pa s, and Figure 9e plots all runs with $d = 165$ km and $\eta_{\min} = 5 \times 10^{18}$ Pa s. Note that plume volume flux increases from Figures 9b to 9e.

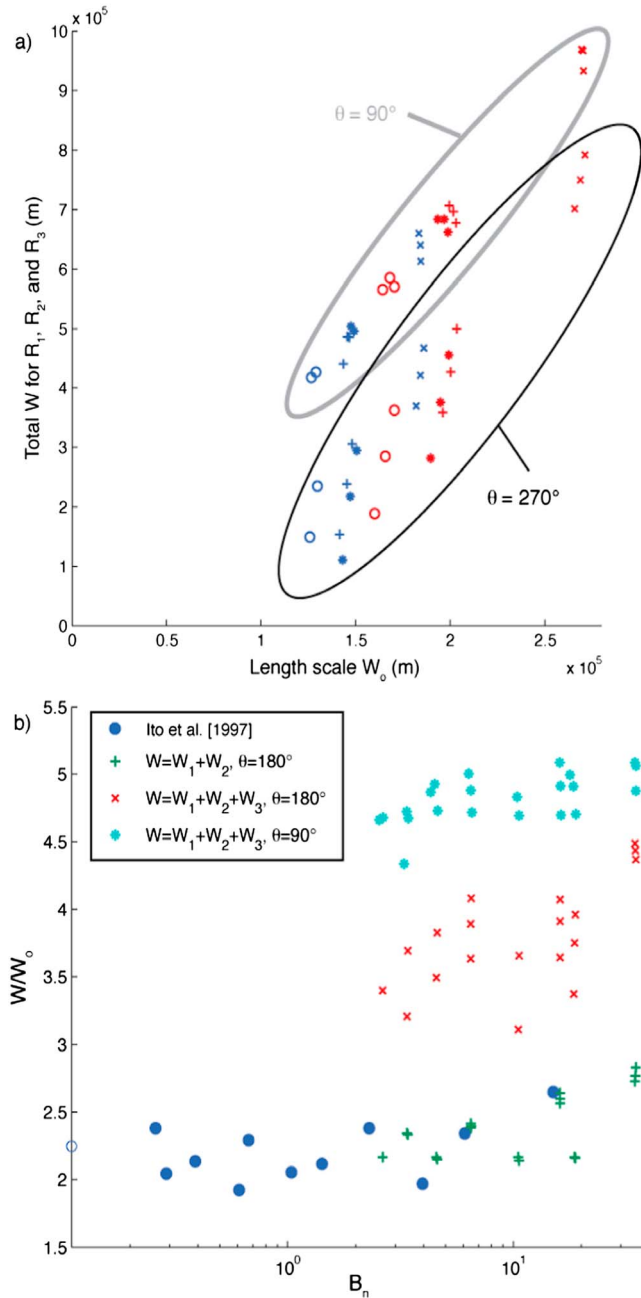


Figure 10. (a) Total waist width $W = W_1 + W_2 + W_3$ as a function of the W_0 length scale for $\theta = 90^\circ$ and $\theta = 270^\circ$. Red and blue symbols represent plumes with diameter (d) of 165 km and 125 km, respectively. Symbols are plus ($\eta_{\min} = 1.5 \times 10^{19}$ Pa s; $A = 1$), circle ($\eta_{\min} = 1.5 \times 10^{19}$ Pa s; $A = [1, 50]$), cross ($\eta_{\min} = 5 \times 10^{18}$ Pa s; $A = 1$), asterisk ($\eta_{\min} = 5 \times 10^{18}$ Pa s; $A = [1, 50]$). All radial distances ($r = 50, 75,$ and 100 km) of the plume conduit from triple junction are plotted with the same color and same symbol. (b) Normalized waist width as a function of buoyancy number for several different definitions of waist width and for two azimuths of the plume conduit. Blue circles show data from Ito et al. [1997], a single-ridge study, for comparison.

spreading R_3 tends to be channeled along the R_3 axis. This channelized flow is promoted because of the large slope of the lithosphere in the direction of spreading, and also because of the relatively low viscosity of the plume compared to the ambient mantle over depths within the partial melting zone. On the other hand, if the same plume conduit is placed in an intraplate location (i.e., $\theta = 270^\circ$), its dispersion in the upper mantle is significantly restricted, in part because of the lack of a ridge axis to promote channelized flow. Plate motion vectors also counter triple junction-directed flow, although it should be noted that a similar argument could be made for a plume to the east of the $R_1 - R_2$ axis (Figure 1c). Finally, the influence of the R_3 axis also helps to explain the smaller sensitivity of the normalized plume area to the parameter r for the $\theta = 90^\circ$ cases, compared to the $\theta = 270^\circ$ cases. Regardless of the value of r for the $\theta = 90^\circ$ cases, the plume conduit encounters a ridge axis, whereas for the $\theta = 270^\circ$ cases, increasing r places the plume in increasing distances away from a spreading branch.

3.5. Comparison of Model Dynamics: Plume–Triple Junction Interaction Versus Plume–Ridge Interaction

The primary goal of this section is to discuss the effect of the existence of the slower spreading ridge (R_3) on waist width (W) and especially to compare results from this study to those found for plume-ridge interaction models. Figure 10a shows total waist width (i.e., $W = W_1 + W_2 + W_3$ or the sum of the waist widths along each of the three ridge axes) as a function of the fundamental length scale of plume-ridge interaction ($W_0 = (Q/u)^{1/2}$), for $\theta = 90^\circ$ and $\theta = 270^\circ$. For both plume azimuths, there is a linear relationship between W and W_0 .

Figure 10b shows total waist width, defined in several different ways, as a function of buoyancy number B_n [Feighner and Richards, 1995], $(Q\rho_0\alpha g\Delta T)/(48\eta_0 U^2)$. Results from Ito et al. [1997]

are plotted for comparison. For cases where $\theta = 180^\circ$ (i.e., a ridge-centered plume), waist widths as defined as $W = W_1 + W_2$ follow the trend from *Ito et al.* [1997]. In contrast, the contribution from triple junction geometry (i.e., the presence of R_3) is seen as elevated values of W when $W = W_1 + W_2 + W_3$. Overall, Figure 10b suggests that the dynamical interactions between a plume and a triple junction may best be explored by defining waist width as a sum of the waist width from R_1 and R_2 , disregarding R_3 . (In the unrealistic and hypothetical case where an arbitrarily large number of ridges meet at a single point near a plume, the waist width defined as the sum of plume anomaly lengths along all of these ridges could approach a very high value.) This definition of waist width also facilitates comparison of plume–triple junction interaction models to earlier studies addressing the interaction of a plume with a single ridge.

4. Application of Modeling Results to Plume–Triple Junction Systems

The results presented above imply that plume–triple junction models can be a useful tool to explore oceanic plateau creation at RRR plate boundary systems. This technique may be particularly informative for settings where ridge geometry is well known but the existence, location, and/or properties of an underlying mantle plume are less well constrained. In the following text, two oceanic plateaus at RRR triple junctions are presented as examples and application of the modeling approach is qualitatively discussed. In the Azores region, ridge geometry can be tightly constrained because the spreading boundaries are extant, but debate exists about the position and nature of the plume. For Shatsky Rise, significant magnetic data constrain the evolution of the Pacific-Izanagi-Farallon triple junction during the time of plateau formation; however, the roughly 150 million years elapsed since the large igneous province began to form means that no direct observational method can be used to characterize the plume that may have been associated with it.

It should be noted that in addition to the Azores and Shatsky Rise cases, there are other plume-affected RRR triple junctions that are candidates for future modeling, after varying aspects of the models like spreading rate and ridge geometry. Examples include Tongareva [*Larson et al.*, 2002; *Viso et al.*, 2005], Bouvet [*Ligi et al.*, 1999; *Georgen and Lin*, 2002], Agulhas [*Hartnady and le Roex*, 1985; *Georgen et al.*, 2001; *Gohl and Uenzelmann-Neben*, 2001], King's Trough [*Searle and Whitmarsh*, 1978; *Mello et al.*, 1999], and Afar [*Haase et al.*, 2000; *Leroy et al.*, 2010].

4.1. Azores Triple Junction

As discussed previously, the Azores triple junction (Figure 2) is formed from two nearly collinear branches of the Mid-Atlantic Ridge with half-spreading rates of ~ 1.1 cm/yr and ~ 1.2 cm/yr; the third branch, the Terceira Rift, intersects the Mid-Atlantic Ridge quasi-orthogonally. *Luis and Miranda* [2008] analyzed magnetic anomalies around the Terceira Rift to study the nature of motion along the plate boundary. Similar to other ultraslow spreading centers with complex geological history, the magnetic anomalies around the Terceira Rift are poorly developed. *Luis and Miranda* [2008] suggested that the Terceira Rift has had a component of divergence for the past 25 million years. In this study, we follow researchers such as *Vogt and Jung* [2004] in describing the Terceira Rift as an ultraslow-spreading ridge with a half rate of ~ 0.3 cm/yr.

Evidence for the existence of a mantle plume near the Azores triple junction can be found in geophysical, geochemical, and seismic tomography data. Time-dependent pulses of magmatism are consistent with topographic V-shaped ridges to the south of the triple junction [*Cannat et al.*, 1999; *Escartin et al.*, 2001]. Seismic tomography studies in the vicinity of the Azores Plateau [e.g., *Montelli et al.*, 2006; *Silveira et al.*, 2006] indicate low-velocity regions in the upper mantle. The Azores region also has geochemical anomalies in seafloor and subaerial basalts compared to mid-ocean ridge basalts [e.g., *Schilling*, 1975; *Dosso et al.*, 1993; *Moreira et al.*, 1999; *Madureira et al.*, 2014], suggesting that there is a different mantle source component in the Azores lavas.

Crustal thicknesses for the Azores Plateau are higher than those for average oceanic crust. From surface wave dispersion measurements, *Searle* [1976] calculated a crustal thickness of ~ 8 km for the central plateau. Using receiver functions, *Silveira et al.* [2010] found that the crust is approximately 20–30 km thick. *Detrick et al.* [1995] used gravity and bathymetry data to determine crustal thicknesses of $> 8 - 9$ km; this is likely to be a maximum estimate because all of the gravity anomaly is attributed to crustal thickness variation (i.e., none is attributed to mantle temperature variation). Treating gravity anomaly data in similar manner, *Gente et al.* [2003] calculated crustal thickness along the Terceira Rift to be at most 5–10 km thicker than along the Mid-Atlantic Ridge, with the highest values around volcanic islands. From studies of admittance, coherence,

and elastic plate behavior, *Luis et al.* [1998] and *Luis and Neves* [2006] calculated a mean crustal thickness for the Azores region of about 10–12 km.

Excess volcanism has occurred for extended periods of geological time in the Azores region. A main phase of Azores Plateau construction started ~10 Ma to ~15 Ma, ending at ~3 Ma to ~7 Ma depending on latitude [*Cannat et al.*, 1999; *Escartin et al.*, 2001]. Since this period of high magmatic production, dominant processes affecting the plateau have included rifting and emplacement of localized volcanic edifices in islands across the archipelago. The present-day islands of the Azores Archipelago (Figure 2) are mostly located to the east of the Mid-Atlantic Ridge, with the exceptions of Flores and Corvo on the west side of the triple junction about 120 km from the Mid-Atlantic Ridge. The lithosphere under Corvo and Flores is approximately 10 Myr in age [*Azevedo et al.*, 1991]. It has been inferred that the initial volcanism creating Corvo and Flores began when the edifices were approximately 70–90 km from the Mid-Atlantic Ridge [*Genske et al.*, 2012]. K/Ar-dated samples go back to approximately 2 Ma and 1.5 Ma for Flores and Corvo, respectively; the youngest eruptive products in the western island complex are geologically recent [*Azevedo et al.*, 1991; *Azevedo and Portugal Ferreira*, 2006; *Genske et al.*, 2012].

As mentioned briefly in section 1.4, observational data from the Azores region display certain asymmetries with respect to the Mid-Atlantic Ridge and the Terceira Rift. For example, elevated seafloor topography can be observed along most of the 550 km Terceira Rift [*Vogt and Jung*, 2004], which is not the case west of the Mid-Atlantic Ridge (Figure 2). Similarly, shallow bathymetry extends farther to the south of the triple junction than to the north [*Detrick et al.*, 1995; *Cannat et al.*, 1999; *Escartin et al.*, 2001; *Goslin and Triatnord Scientific Party*, 1999; *Maia et al.*, 2007] (Figure 2). According to these data the maximum extent of the Azores plume effect toward the north is close to Kurchatov Fracture Zone (Figure 2), approximately 120 km from the triple junction [*Goslin and Triatnord Scientific Party*, 1999; *Maia et al.*, 2007]. To the south, anomalies can be observed to the Atlantis Fracture Zone [*Detrick et al.*, 1995; *Thibaud et al.*, 1998] some ~1500 km away from the triple junction. Gravity data, geochemical data, and tomography-based modeling of bathymetry and seafloor stresses reinforce these observations of asymmetry [*Dosso et al.*, 1993; *Detrick et al.*, 1995; *Yu et al.*, 1997; *Thibaud et al.*, 1998; *Goslin and Triatnord Scientific Party*, 1999; *Maia et al.*, 2007; *Adam et al.*, 2013]. The shallowest point along the Mid-Atlantic Ridge in the Azores region is approximately 100 km south of the triple junction. From that point, seafloor depth increases by approximately 1–2 km to ridge segments outside of Azores plume influence (e.g., north of the Kurchatov Fracture Zone).

4.1.1. Comparison of Modeling Results to Observational Data

Although many studies assume an Azores plume conduit in the general vicinity of Faial and Pico islands, the precise conduit location in the deep upper mantle is in fact a matter of some debate. Depending upon the data set under consideration, suggestions include northeast of Terceira Island [e.g., *Yang et al.*, 2006] as well as locations ranging from west of the Mid-Atlantic Ridge to ~100 km south of Faial and Pico islands [*Shorttle et al.*, 2010, and references therein]. Although the numerical results described above were produced using a fairly rudimentary ridge geometry and simple (i.e., not time dependent) spreading history, comparison of the observational data to model results can provide some insight into the position of the plume with respect to the triple junction, to narrow down the range of likely plume azimuths.

Focusing on the predicted topographic variations along the $R_1 - R_2$ axis (Figures 6 and 7), models for which the azimuth of the plume conduit was 135° , 180° , or 225° seem to produce seafloor topography variations that are consistent with depth trends along the Mid-Atlantic Ridge (Figure 2), which are asymmetric in a north-south direction with respect to the triple junction. In contrast, models with $\theta = 90^\circ$ and $\theta = 270^\circ$ produce seafloor depth anomalies that are roughly symmetric about the triple junction point along the $R_1 - R_2$ axis, rather than extending to a greater distance to the south of the triple junction along R_2 . When $\theta = 315^\circ$, the peak in seafloor depth is shifted to the north of the triple junction along R_2 , also inconsistent with observations. Therefore, the pattern of depth anomalies along the Mid-Atlantic Ridge would seem to suggest that $\theta = 135^\circ$, 180° , or 225° . However, these preferred azimuths can be narrowed down by considering seafloor depth variations to the west of the Mid-Atlantic Ridge. Although not shown, models with $\theta \geq 225^\circ$ predict seafloor that is shallower to the west of the $R_1 - R_2$ axis than along R_3 , a pattern that is not consistent with observed depths. The remaining azimuths are $\theta = 135^\circ$ and $\theta = 180^\circ$.

Focusing on the east-west plane along which R_3 is located, dynamic topography variations are greater for smaller plume azimuths (Figure 7). Studies such as *Georgen and Sankar* [2010] and *Adam et al.* [2013] suggest

that the regional depth anomaly associated with the swell is approximately 1–2 km in amplitude. Runs shown in Figure 7b ($\theta = 90^\circ$) and 7d ($\theta = 135^\circ$) are most consistent with this observation. However, for cases with $\theta = 90^\circ$ in Figures 3–5, relatively little plume material is advected to the west of the $R_1 - R_2$ axis for smaller plumes or plumes located at larger distances from the triple junction. Thus, these cases do not appear to be in agreement with recent volcanic activity at Flores and Corvo islands. Overall, therefore, model results tend to point to an off-axis plume location in between the Terceira Rift and the southern branch of the Mid-Atlantic Ridge.

Additional constraint on modeled parameters like plume diameter and calculated quantities such as buoyancy flux could come from seismic data. However, a challenge in comparing the model-predicted crustal thickness variations to seismic observations is the relative coarseness of currently available seismic crustal thickness measurements. Because of instrument placement considerations, available seismic crustal thickness data for the Azores region tend to be biased toward measurements for the islands, which are likely locally thicker and not representative of regional variation throughout the plateau. Ideally, to compare model results with seismic data, there would be crustal thickness measurements along all three branches of the triple junction with spacing at the segment-scale level (~10–100 km). Such measurements would constrain both the magnitude of crustal thickness variation (e.g., Figures 8c and 8d) and also the gradients from areas of thickened crust to areas with average crustal thickness (e.g., Figures 8a and 8b). Calculations of crustal thickness using elastic plate behavior generally do not provide such fine-scale resolution. Although several studies have used gravity data to calculate maps of crustal thickness variations for the Azores region [e.g., Gente *et al.*, 2003; Georgen and Sankar, 2010], interpretation of gravity anomalies in terms of crustal thickness variations is inherently dependent on several important assumptions.

4.1.2. Azores Triple Junction: Future Modeling Work

It is encouraging that a subset of the numerical model runs yield predicted seafloor depth anomalies that are qualitatively similar to observational data for the Azores region, particularly considering that the model domain and numerical approach capture only some aspects of the Azores plume-ridge system. These aspects include present-day spreading rate and the general orientation of the three ridge branches. Future investigations can modify the basic model domain and numerical treatment to make calculations more specific to the geology and evolution of the Azores setting. For example, studies can add time-dependent spreading history, since the Terceira Rift has had a component of divergence for only a relatively short time. Studies can also incorporate movement of the triple junction with respect to the plume, including a significant jump in triple junction location that occurred approximately 40 Ma [e.g., Searle, 1980]. Another important component in future models will be treatment of the Azores plume not just as a thermal feature, but as a chemical anomaly as well. Numerous studies [e.g., Bonatti, 1990; Asimow *et al.*, 2004] have addressed the role of chemical heterogeneity and mantle fertility variations in generating Azores magmatism. It is possible that plume-triple junction models that treat the Azores mantle anomaly as a thermochemical plume will predict more complex variability in patterns of seafloor depth than those described above.

One potentially promising area for future work would be to calculate the three-dimensional seismic velocity structure corresponding to each of the model runs, to compare to available regional and global seismic tomography models [e.g., Yang *et al.*, 2006; Montelli *et al.*, 2006; Silveira *et al.*, 2006; Ritsema *et al.*, 2011]. It is important to note that, as pointed out by studies such as Silveira *et al.* [2006], fairly considerable variability exists amongst these models. This results in some ambiguity in defining the volume of the mantle occupied by the plume structure, over both short and long wavelengths. Thus, evaluating numerical modeling against seismic tomography might best be performed by first completing the additional modeling work described in the previous paragraph and assessing which of these new models best match data such as seafloor depth. The preferred model(s) could then be compared to each of the existing seismic tomography models.

4.2. Shatsky Rise and Pacific-Izanagi-Farallon Triple Junction

Application of this modeling may also lend insight into the processes that created Shatsky Rise. Shatsky Rise is a large oceanic plateau of Jurassic-Cretaceous age located in the northwest Pacific [Nakanishi *et al.*, 1999; Mahoney *et al.*, 2005]. Therefore, unlike the Azores Plateau, Shatsky Rise no longer sits above the mantle plume that may have been involved in its formation. The properties of this postulated plume, and its location with respect to the rise, remain an open question.

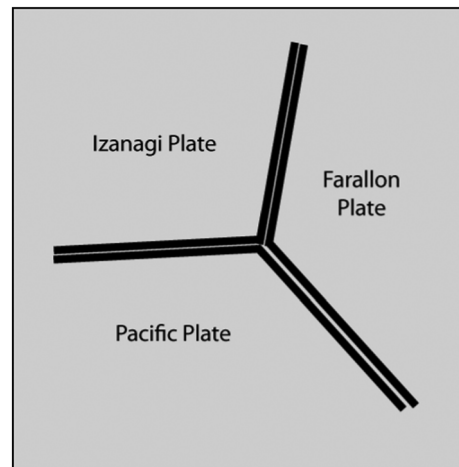


Figure 11. Schematic representation of the geometry of the Pacific-Izanagi-Farallon triple junction at the time of Shatsky Rise formation. Ridge geometry is after *Nakanishi et al.* [1999].

Shatsky Rise contains three massifs, with the age and size of the massifs decreasing from Tamu Massif in the southwest, to Ori Massif in the central portion of the plateau, to Shirshov Massif in the northeast [*Sager and Han, 1993*]. Papanin Ridge, a comparatively smaller feature, defines the northern portion of the large igneous province. Several lines of evidence suggest Shatsky Rise was emplaced in a near-ridge environment. For example, gravity analysis indicates Shatsky Rise formed on young, weak lithosphere [*Van Ark and Lin, 2004*]. $^{40}\text{Ar}/^{39}\text{Ar}$ dates for two samples in the southern portion of Tamu Massif are 144 ± 0.8 Ma [*Mahoney et al., 2005*], close to the age of the seafloor surrounding this portion of the plateau. Magnetic isochron patterns, including the Japanese and Hawaiian lineations, indicate that Shatsky Rise was created at or near an RRR triple junction consisting of the Pacific, Izanagi, and Farallon plates [*Nakanishi et al., 1989*].

The size of the rise is consistent with mantle plume involvement in its formation [*Nakanishi et al., 1989*].

Seismic data indicate crustal thicknesses up to approximately 30 km [*Den et al., 1969; Gettrust et al., 1980; Korenaga and Sager, 2012*]. These data are roughly consistent with maximum gravity-derived crustal thickness values of 19 km, which were made by attributing all residual mantle Bouguer anomaly signal to variations in crustal thickness, rather than mantle density [*Van Ark and Lin, 2004*]. Magnetic data and age constraints from drilling suggest that Tamu Massif was largely constructed between anomalies M21 and M19 [*Sager and Han, 1993; Sager, 2005*]. The duration of volcanism, combined with magnetic modeling and geometric arguments about the massif's volume, yields an emplacement rate of 1.2–4.6 km³/yr [*Sager and Han, 1993; Sager, 2005*]. This rate places the southern portion of Shatsky Rise toward the midrange of large igneous province fluxes [*Coffin and Eldholm, 1994*]. Emplacement rates appear to decrease northward through the Ori and Shirshov massifs and drop off considerably for the Papanin Ridge [*Sager et al., 1999*]. The sequence of massifs could be consistent with consecutive jumps of the Pacific-Izanagi-Farallon triple junction following the location of a mantle plume [*Sager et al., 1988; Nakanishi et al., 1999*] together with plume flux that decreased over time.

In a future study, the modeling approach developed in this investigation could be used to better understand the properties and time-dependent evolution of the plume that might have been active under the massifs of Shatsky Rise. A necessary initial step would be to redesign the model domain for the Pacific-Izanagi-Farallon RRR system, which had a configuration closer to a “Y” shape than a “T” shape (Figure 11). The domain would also need to be larger to accommodate the intermediate to fast-spreading rates of the ridges of the Pacific-Izanagi-Farallon triple junction [*Sager et al., 1988*] and the possibly higher volume flux of the plume.

One of the persistent questions surrounding the formation of Shatsky Rise is the relative importance of plate boundary and plume processes in generating excess magmatism. As mentioned in section 1.4, *Georgen and Lin* [2002] calculated that when a triple junction contains an ultraslow- or slow-spreading branch, significant crustal thickness increases may occur along this branch in the vicinity of the triple junction. However, for a triple junction composed of intermediate- and fast-spreading ridges, *Georgen and Lin* [2002] found relatively little crustal thickening caused by the RRR geometry alone. Although the model of *Georgen and Lin* [2002] used a T-shaped triple junction and this result would need to be verified for Y-shaped geometry, these results could imply that plate boundary geometry itself (i.e., plate boundary configuration in the absence of a mantle plume) did not have a significant impact on crustal thickness variations in Shatsky Rise.

5. Conclusions

This study uses a series of finite element models to calculate the interaction of a mantle plume and an RRR triple junction in a parameter space investigation-type approach. The model runs vary plume location (azimuthal position around the triple junction as well as distance between the plume and the triple junction),

plume diameter, the ratio of ambient mantle viscosity to plume viscosity, and the use of dehydration rheology in calculating viscosity. These models establish a framework for understanding the dynamics of plume–triple junction interactions. More specifically, the model results quantify how plume-related anomalies in mantle temperature pattern, seafloor depth, and crustal thickness depend on the specific combination of parameters. As an example, this investigation assesses the effect of conduit position by calculating a quantity called normalized area, which is defined to be the spatial dispersion of a given plume at specific depth (here selected to be 50 km) divided by the area occupied by the same plume when it is located under the triple junction. For some cases, such as for high-flux plumes and plumes that are located along the slowest-spreading ridge branch R_3 , normalized area is approximately 1. However, in other cases, such as where a low-flux plume is centered in an intraplate position 100 km from the triple junction, normalized area is just 0.55.

When plume–triple junction models incorporate dehydration rheology, plume advection is restricted to smaller regions in the shallow mantle compared to cases when viscosity is dependent only on temperature and pressure. Plume advection more closely follows the lithosphere–asthenosphere boundary in the cases without dehydration compared to those where viscosity increases at the depth at which melting begins. Additionally, for cases with dehydration, there are decreases in the amplitude and wavelength of axial anomalies in seafloor topography and crustal thickness. These results are consistent with several earlier studies of the interaction of a plume with a single ridge axis that used dehydration-dependent mantle rheology.

One implication of this investigation is that, for oceanic plateaus that formed in the vicinity of an RRR triple junction, this modeling approach can be used to constrain properties of an underlying mantle plume that are not directly observable. This approach would be most informative when abundant data are available to delineate ridge axis geometry and the areal extent, shape, and volume of the oceanic plateau. Two examples of such systems are the present-day Azores Plateau and Shatsky Rise, which formed in the Jurassic–Cretaceous Pacific Ocean.

Acknowledgments

This manuscript benefitted greatly from the careful reviews of M. Bizimis, N. Mitchell, two anonymous reviewers, and the Associate Editor. Portions of Dordevic's graduate program of study were supported through National Science Foundation (NSF) CCLI-0837040, NSF TUES-1022755, NSF GEO-1034643, and a Google Faculty Research Award. Earlier stages of this work were supported by NSF OCE-0550250 and NSF OCE-0936981 to Georgen. Models were calculated using COMSOL software (www.comsol.com).

References

- Adam, C., P. Madureira, J. M. Miranda, N. Lourenco, M. Yoshida, and D. Fitenz (2013), Mantle dynamics and characteristics of the Azores plateau, *Earth Planet. Sci. Lett.*, *362*, 258–271.
- Albers, M., and U. Christensen (2001), Channeling of plume flow beneath mid-ocean ridges, *Earth Planet. Sci. Lett.*, *187*, 207–220.
- Asimow, P. D., J. E. Dixon, and C. H. Langmuir (2004), A hydrous melting and fractionation model for mid-ocean ridge basalt: Application to the Mid-Atlantic Ridge near the Azores, *Geochem. Geophys. Geosyst.*, *5*, Q01E16, doi:10.1029/2003GC000568.
- Azevedo, J. M. M., and M. R. Portugal Ferreira (2006), The volcanotectonic evolution of Flores Island, Azores, *J. Volcanol. Geotherm. Res.*, *156*, 90–102.
- Azevedo, J. M. M., M. P. Ferreira, and J. A. Martins (1991), The emergent volcanism of Flores island, Azores (Portugal), *Arquipelago*, *9*, 37–46.
- Barruol, G., and F. R. Fontaine (2013), Mantle flow beneath La Reunion hotspot track from SKS splitting, *Earth Planet. Sci. Lett.*, *362*, 108–121.
- Bonatti, E. (1990), Not so hot "hot spots" in the oceanic mantle, *Science*, *250*, 107–111.
- Braun, M. G., G. Hirth, and E. M. Parmentier (2000), The effects of deep damp melting on mantle flow and melt generation beneath mid-ocean ridges, *Earth Planet. Sci. Lett.*, *176*, 339–356.
- Canales, J. P., G. Ito, R. S. Detrick, and J. Sinton (2002), Crustal thickness along the western Galapagos Spreading Center and the compensation of the Galapagos hotspot swell, *Earth Planet. Sci. Lett.*, *203*, 311–327.
- Cannat, M., et al. (1999), Mid-Atlantic Ridge–Azores hotspot interactions: Along-axis migration of a hotspot-derived event of enhanced magmatism 10 to 4 Ma, *Earth Planet. Sci. Lett.*, *173*, 257–269.
- Coffin, M. F., and O. Eldholm (1994), Large igneous provinces: Crustal structure, dimensions, and external consequences, *Rev. Geophys.*, *32*, 1–36.
- Delorey, D., R. A. Dunn, and J. B. Gaherty (2007), Surface wave tomography of the upper mantle beneath the Reykjanes Ridge with implications for ridge–hotspot interaction, *J. Geophys. Res.*, *112*, B08313, doi:10.1029/2006JB004785.
- Den, N., W. J. Ludwig, S. Murauchi, J. I. Ewing, H. Hotta, N. T. Edgar, T. Yoshii, T. Asanuma, K. Hagiwra, and T. Sato (1969), Seismic refraction measurements in the northwest Pacific Basin, *J. Geophys. Res.*, *74*, 1421–1434.
- Detrick, R. S., H. D. Needham, and V. Renard (1995), Gravity anomalies and crustal thickness variations along the Mid-Atlantic Ridge between 33°N and 40°N, *J. Geophys. Res.*, *100*, 3767–3787.
- Detrick, R. S., J. M. Sinton, G. Ito, J. P. Canales, M. Behn, T. Blacic, B. Cushman, J. E. Dixon, D. W. Graham, and J. Mahoney (2002), Correlated geophysical, geochemical, and volcanological manifestations of plume–ridge interaction along the Galapagos Spreading Center, *Geochem. Geophys. Geosyst.*, *3*(10), 8501, doi:10.1029/2002GC000350.
- Dick, H. J. B., J. Lin, and H. Schouten (2003), An ultraslow-spreading class of ocean ridge, *Nature*, *426*, 405–412.
- Dosso, L., H. Bougault, and J.-L. Joron (1993), Geochemical morphology of the North Mid-Atlantic Ridge, 10 degrees–24 degrees N: Trace element–isotope complementarity, *Earth Planet. Sci. Lett.*, *120*, 443–462.
- Escartin, J., M. Cannat, G. Pouliquen, A. Rabain, and J. Lin (2001), Crustal thickness of V-shaped ridges south of the Azores: Interaction of the Mid-Atlantic Ridge (36°–39°N) and the Azores hot spot, *J. Geophys. Res.*, *106*, 21,719–21,735.
- Feighner, M. A., and M. A. Richards (1995), The fluid dynamics of plume–ridge and plume–plate interactions: An experimental investigation, *Earth Planet. Sci. Lett.*, *129*, 171–182.
- Genske, F. S., S. P. Turner, C. Beier, and B. F. Schaefer (2012), The petrology and geochemistry of lavas from the western Azores islands of Flores and Corvo, *J. Petrol.*, *53*(8), 1673–1708.

- Gente, P., J. Dymant, M. Maia, and J. Goslin (2003), Interaction between the Mid-Atlantic Ridge and the Azores hot spot during the last 85 Myr: Emplacement and rifting of the hot spot-derived plateaus, *Geochem. Geophys. Geosyst.*, *4*(10), 8514, doi:10.1029/2003GC000527.
- Georgen, J., and J. Lin (2002), Three-dimensional passive flow and temperature structure beneath oceanic ridge-ridge-ridge triple junctions, *Earth Planet. Sci. Lett.*, *204*, 115–132.
- Georgen, J. E. (2008), Mantle flow and melting beneath oceanic ridge-ridge-ridge triple junctions, *Earth Planet. Sci. Lett.*, *270*, 231–240.
- Georgen, J. E. (2011), Lithospheric control on the spatial pattern of Azores hotspot seafloor anomalies: Constraints from a model of plume-triple junction interaction, *Geophys. Res. Lett.*, *38*, L19305, doi:10.1029/2011GL048742.
- Georgen, J. E. (2014), Interaction of a mantle plume and a segmented mid-ocean ridge: Results from numerical modeling, *Earth Planet. Sci. Lett.*, *392*, 113–120.
- Georgen, J. E., and R. D. Sankar (2010), Effects of ridge geometry on mantle dynamics in an oceanic triple junction region: Implications for the Azores Plateau, *Earth Planet. Sci. Lett.*, *298*, 23–34.
- Georgen, J. E., J. Lin, and H. J. B. Dick (2001), Evidence from gravity anomalies for interactions of the Marion and Bouvet hotspots with the Southwest Indian Ridge: Effects of transform offsets, *Earth Planet. Sci. Lett.*, *187*, 283–300.
- Gettrust, J. F., K. Furukawa, and L. W. Kroenke (1980), Crustal structure of the Shatsky Rise from seismic refraction measurements, *J. Geophys. Res.*, *85*, 5411–5415.
- Gohl, K., and G. Uenzelmann-Neben (2001), The crustal role of the Agulhas Plateau, southwest Indian Ocean: Evidence from seismic profiling, *Geophys. J. Int.*, *144*(3), 632–646.
- Goslin, J., and Triatnord Scientific Party (1999), Extent of Azores plume influence on the Mid-Atlantic Ridge north of the hotspot, *Geology*, *27*, 991–994.
- Haase, K. M., R. Mühe, and P. Stoffers (2000), Magmatism during extension of the lithosphere: Geochemical constraints from lavas of the Shaban Deep, northern Red Sea, *Chem. Geol.*, *166*(3), 225–239.
- Hall, P. S., and C. Kincaid (2003), Melting, dehydration, and the dynamics of off-axis plume-ridge interaction, *Geochem. Geophys. Geosyst.*, *4*(9), 8510, doi:10.1029/2003GC000567.
- Hartnady, C. J. H., and A. P. le Roex (1985), Southern ocean hotspot tracks and the Cenozoic absolute motion of the African, Antarctic, and South American plates, *Earth Planet. Sci. Lett.*, *75*, 245–257.
- Hirth, G., and D. L. Kohlstedt (1996), Water in the oceanic upper mantle: Implications for rheology, melt extraction and the evolution of the lithosphere, *Earth Planet. Sci. Lett.*, *144*, 93–108.
- Howell, S. M., G. Ito, A. Brevik, A. Rai, R. Mjelde, B. Hanan, K. Sayit, and P. Vogt (2014), The origin of the asymmetry in the Iceland hotspot along the Mid-Atlantic Ridge from continental breakup to present-day, *Earth Planet. Sci. Lett.*, *392*, 143–153.
- Ito, G., J. Lin, and C. W. Gable (1996), Dynamics of mantle flow and melting at a ridge-centered hotspot: Iceland and the Mid-Atlantic Ridge, *Earth Planet. Sci. Lett.*, *144*, 53–74.
- Ito, G., J. Lin, and C. Gable (1997), Interaction of mantle plumes and migrating mid-ocean ridges: Implications for the Galapagos plume-ridge system, *J. Geophys. Res.*, *102*, 17,403–17,417.
- Ito, G., Y. Shen, G. Hirth, and C. Wolfe (1999), Mantle flow, melting, and dehydration of the Iceland mantle plume, *Earth Planet. Sci. Lett.*, *165*, 81–96.
- Ito, G., J. Lin, and D. Graham (2003), Observational and theoretical studies of the dynamics of mantle plume-mid-ocean ridge interaction, *Rev. Geophys.*, *41*(4), 1017, doi:10.1029/2002RG000117.
- Ito, G., R. Dunn, and A. Li (2015), The origin of shear wave splitting beneath Iceland, *Geophys. J. Int.*, *201*(3), 1297–1312.
- King, S. D., and C. Adam (2014), Hotspot swells revisited, *Phys. Earth Planet. Inter.*, *235*, 66–83.
- Klein, E. M., D. K. Smith, C. M. Williams, and H. Schouten (2005), Counter-rotating microplates at the Galapagos triple junction (2005), *Nature*, *433*, 855–858.
- Korenaga, J., and W. W. Sager (2012), Seismic tomography of Shatsky Rise by adaptive importance sampling, *J. Geophys. Res.*, *117*, B10404, doi:10.1029/2012JB009524.
- Larson, R. L., R. A. Pockalny, R. F. Viso, E. Erba, L. J. Abrams, B. P. Luyendyk, J. M. Stock, and R. W. Clayton (2002), Mid-Cretaceous tectonic evolution of the Tongareva triple junction in the southwestern Pacific Basin, *Geology*, *30*, 67–70.
- Leroy, S., E. d'Acremont, C. Tiberi, C. Basuyau, J. Autin, F. Lucazeau, and H. Sloan (2010), Recent off-axis volcanism in the eastern Gulf of Aden: Implications for plume-ridge interaction, *Earth Planet. Sci. Lett.*, *293*, 140–153.
- Ligi, M., E. Bonatti, G. Bortoluzzi, G. Carrara, P. Fabretti, D. Gilod, A. A. Peyve, S. Skolotnev, and N. Turko (1999), Bouvet triple junction in the South Atlantic: Geology and evolution, *J. Geophys. Res.*, *104*, 29,365–29,385.
- Luis, J., J. Miranda, A. Galdeano, P. Patriat, J. Rossignol, and L. Mendes-Victor (1994), The Azores triple junction evolution since 10 Ma from an aeromagnetic survey of the Mid-Atlantic Ridge, *Earth Planet. Sci. Lett.*, *125*, 439–459.
- Luis, J., J. Miranda, A. Galdeano, and P. Patriat (1998), Constraints on the structure of the Azores spreading center from gravity data, *Mar. Geophys. Res.*, *20*, 157–170.
- Luis, J. F., and J. M. Miranda (2008), Reevaluation of magnetic chrons in the North Atlantic between 35°N and 47°N: Implications for the formation of the Azores triple junction and associated plateau, *J. Geophys. Res.*, *113*, B10105, doi:10.1029/2007JB005573.
- Luis, J. F., and M. C. Neves (2006), The isostatic compensation of the Azores Plateau: A 3D admittance and coherence analysis, *J. Volcanol. Geotherm. Res.*, *156*, 10–22.
- Madureira, P., M. Moreira, J. Mata, J. C. Nunes, C. Gautheron, N. Lorenco, R. Carvalho, and M. Pinto de Abreu (2014), Helium isotope systematics in the vicinity of the Azores triple junction: Constraints on the Azores geodynamics, *Chem. Geol.*, *372*, 62–71.
- Mahoney, J., R. A. Duncan, M. L. G. Tejada, W. W. Sager, and T. J. Bralower (2005), Jurassic-Cretaceous boundary age and mid-ocean-ridge-type mantle source for Shatsky Rise, *Geology*, *33*, 185–188.
- Maia, M., J. Goslin, and P. Gente (2007), Evolution of the accretion processes along the Mid-Atlantic ridge north of the Azores since 5.5 Ma: An insight into the interactions between the ridge and the plume, *Geochem. Geophys. Geosyst.*, *8*, Q03013, doi:10.1029/2006GC001318.
- Marquart, G., H. Schmeling, and O. Cadek (2007), Dynamic models for mantle flow and seismic anisotropy in the North Atlantic region and comparison with observations, *Geochem. Geophys. Geosyst.*, *8*, Q02008, doi:10.1029/2006GC001359.
- McKenzie, D., and W. J. Morgan (1969), Evolution of triple junctions, *Nature*, *224*, 122–133.
- McKenzie, D. P., and M. Bickle (1988), The volume and composition of melt generated by extension of the lithosphere, *J. Petrol.*, *25*, 625–679.
- Mello, S. L. M., J. R. Cann, and C. M. R. Fowler (1999), Anomalous mantle at 45°N Mid-Atlantic Ridge?, *J. Geophys. Res.*, *104*(B12), 29,335–29,349.
- Miranda, J. M., J. F. Luis, N. Lourenco, and J. Goslin (2014), Distributed deformation close to the Azores Triple "Point", *Mar. Geol.*, *355*, 27–35.
- Mitchell, N., and L. Parson (1993), The tectonic evolution of the Indian Ocean triple junction, anomaly 6 to present, *J. Geophys. Res.*, *98*, 1793–1812.
- Mittelstaedt, E., S. Soule, K. Harpp, D. Fornari, C. McKee, M. Tivey, D. Geist, M. D. Kurz, C. Sinton, and C. Mello (2012), Multiple expressions of plume-ridge interaction in the Galapagos: Volcanic lineaments and ridge jumps, *Geochem. Geophys. Geosyst.*, *13*, Q05018, doi:10.1029/2012GC004093.
- Montelli, R., G. Nolet, F. A. Dahlen, and G. Masters (2006), A catalogue of deep mantle plumes: New results from finite-frequency tomography, *Geochem. Geophys. Geosyst.*, *7*, Q11007, doi:10.1029/2006GC001248.

- Moreira, M., R. Doucelance, M. D. Kurz, B. Dupré, and C. J. Allègre (1999), Helium and lead isotope geochemistry of the Azores Archipelago, *Earth Planet. Sci. Lett.*, *169*(1), 189–205.
- Morgan, W. J. (1971), Convection plumes in the lower mantle, *Nature*, *230*, 42–43.
- Morgan, W. J. (1972), Deep mantle convection plumes and plate motions, *AAPG Bull.*, *56*, 203–213.
- Morgan, W. J. (1981), *Hotspot Tracks and the Opening of the Atlantic and Indian Oceans*, vol. 7, chap. 13, pp. 443–487, Intersci., New York.
- Nakanishi, M., K. Tamaki, and K. Kobayashi (1989), Mesozoic magnetic anomaly lineations and seafloor spreading history of the northwestern Pacific, *J. Geophys. Res.*, *94*, 15,437–15,462.
- Nakanishi, M., W. W. Sager, and A. Klaus (1999), Magnetic lineations within Shatsky Rise, northwest Pacific Ocean: Implications for hot spot-triple junction interaction and oceanic plateau formation, *J. Geophys. Res.*, *104*, 7539–7556.
- Olson, P. (1990), Hot spots, swells and mantle plumes, in *Magma Transport and Storage*, edited by M. P. Ryan, pp. 33–51, John Wiley, Chichester, U.K.
- Putirka, K. D., M. Perfit, F. J. Ryerson, and M. G. Jackson (2007), Ambient and excess mantle temperatures, olivine thermometry, and active vs. passive upwelling, *Chem. Geol.*, *241*, 177–206.
- Rabinowicz, M., M. Calvet, and M. J. Toplis (2012), Possible layering of mantle convection at the top of the Iceland Hotspot: A crosscheck between 3-D numerical models and gravimetric, seismic and petrological data, *Geophys. J. Int.*, *188*(1), 35–60.
- Reid, I., and H. R. Jackson (1981), Oceanic spreading rate and crustal thickness, *Mar. Geophys. Res.*, *5*, 165–172.
- Ribe, N., U. Christensen, and J. Theissing (1995), The dynamics of plume-ridge interaction, 1 Ridge-centered plumes, *Earth Planet. Sci. Lett.*, *134*, 155.
- Ribe, N. M. (1996), The dynamics of plume-ridge interaction 2. Off-ridge plumes, *J. Geophys. Res.*, *101*, 16,195–16,204.
- Ribe, N. M., and W. L. Delattre (1998), The dynamics of plume—ridge interaction—III. The effects of ridge migration, *Geophys. J. Int.*, *133*(3), 511–518.
- Ritsema, J., A. Deuss, H. J. van Heijst, and J. H. Woodhouse (2011), S40RTS: A degree-40 shear-velocity model for the mantle from new Rayleigh wave dispersion, teleseismic traveltimes and normal-mode splitting function measurements, *Geophys. J. Int.*, *3*, 1223–1236.
- Sager, W. W. (2005), What built Shatsky Rise, a mantle plume or ridge processes?, in *Plates, Plumes, and Paradigms*, edited by G. R. Foulger et al., *Geol. Soc. Am. Spec. Pap.*, *388*, 721–733.
- Sager, W. W., and H. Han (1993), Rapid formation of the Shatsky Rise oceanic plateau inferred from its magnetic anomaly, *Nature*, *364*, 610–613.
- Sager, W. W., D. W. Handschumacher, T. W. C. Hilde, and D. R. Bracey (1988), Tectonic evolution of the northern Pacific plate and Pacific-Farallon-Izanagi triple junction in the late Jurassic and early Cretaceous (M21-M10), *Tectonophysics*, *155*, 345–364.
- Sager, W. W., J. Kim, A. Klaus, M. Nakanishi, and L. M. Khankishieva (1999), Bathymetry of Shatsky Rise, northwest Pacific Ocean: Implications for ocean plateau development at a triple junction, *J. Geophys. Res.*, *104*, 7557–7576.
- Schilling, J. G. (1975), Azores mantle blob: Rare-Earth evidence, *Earth Planet. Sci. Lett.*, *25*(2), 103–115.
- Sclater, J., C. Bowin, R. Hey, H. Hoskins, J. Peirce, J. Phillips, and C. Tapscott (1976), The Bouvet triple junction, *J. Geophys. Res.*, *81*, 1857–1869.
- Searle, R. (1980), Tectonic pattern of the Azores spreading center and triple junction, *Earth Planet. Sci. Lett.*, *51*, 415–434.
- Searle, R. C. (1976), Lithospheric structure of the Azores Plateau from Rayleigh-wave dispersion, *Geophys. J. R. Astron. Soc.*, *44*, 537–546.
- Searle, R. C., and J. Francheteau (1986), Morphology and tectonics of the Galapagos triple junction, *Mar. Geophys. Res.*, *8*, 95–129.
- Searle, R. C., and R. B. Whitmarsh (1978), The structure of King's Trough, Northeast Atlantic, from bathymetric, seismic and gravity studies, *Geophys. J. Int.*, *53*(2), 259–287.
- Shotttle, O., J. MacLennan, and S. M. Jones (2010), Control of the symmetry of plume-ridge interaction by spreading ridge geometry, *Geochem. Geophys. Geosyst.*, *11*, Q0AC05, doi:10.1029/2009GC002986.
- Silveira, G., E. Stutzmann, A. Davaille, J.-P. Montagner, L. Mendes-Victor, and A. Sebai (2006), Azores hotspot signature in the upper mantle, *J. Volcanol. Geotherm. Res.*, *156*, 23–34.
- Silveira, G., L. Vinnik, E. Stutzmann, V. Farra, S. Kiselev, and I. Morais (2010), Stratification of the Earth beneath the Azores from P and S receiver functions, *Earth Planet. Sci. Lett.*, *299*, 91–103.
- Sleep, N. H. (1990), Hotspots and mantle plumes: Some phenomenology, *J. Geophys. Res.*, *95*, 6715–6936.
- Smith, W. H., and D. T. Sandwell (1997), Global sea floor topography from satellite altimetry and ship depth soundings, *Science*, *277*(5334), 1956–1962.
- Sparks, D. W., and E. M. Parmentier (1993), The structure of three-dimensional convection beneath oceanic spreading centers, *Geophys. J. Int.*, *112*, 19,727–19,728.
- Thibaud, R., P. Gente, and M. Maia (1998), A systematic analysis of the Mid-Atlantic Ridge morphology and gravity between 15°N and 40°N: Constraints of the thermal structure, *J. Geophys. Res.*, *103*, 24,223–24,243.
- Van Ark, E., and J. Lin (2004), Time variation in igneous volume flux of the Hawaii-Emperor hot spot seamount chain, *J. Geophys. Res.*, *109*, B11401, doi:10.1029/2003JB002949.
- van Keken, P. E., et al. (2008), A community benchmark for subduction zone modeling, *Phys. Earth Planet. Int.*, *171*(1), 187–197.
- Vidal, V., and A. Bonneville (2004), Variations of the Hawaiian hot spot activity revealed by variations in the magma production rate, *J. Geophys. Res.*, *109*, B03104, doi:10.1029/2003JB002559.
- Viso, R., R. L. Larson, and R. A. Pockalny (2005), Tectonic evolution of the Pacific-Phoenix-Farallon triple junction in the South Pacific Ocean, *Earth Planet. Sci. Lett.*, *233*, 179–194.
- Vogt, P. R., and W. Y. Jung (2004), The Terceira Rift as a hyper-slow, hotspot-dominated oblique spreading axis: A comparison with other slow-spreading plate boundaries, *Earth Planet. Sci. Lett.*, *218*, 77–90.
- Wolfe, C., I. T. Bjarnason, J. C. VanDecar, and S. C. Solomon (1997), Seismic structure of the Iceland mantle plume, *Nature*, *385*, 245–247.
- Wolfe, C. J., S. C. Solomon, G. Laske, J. A. Collins, R. S. Detrick, J. A. Orcutt, D. Bercovici, and E. H. Hauri (2009), Mantle shear-wave velocity structure beneath the Hawaiian hot spot, *Science*, *326*, 1388–1390.
- Xue, M., and R. M. Allen (2005), Asthenospheric channeling of the Icelandic upwelling: Evidence from seismic anisotropy, *Earth Planet. Sci. Lett.*, *235*, 167–182.
- Yang, T., Y. Shen, S. van der Lee, S. C. Solomon, and S.-H. Hung (2006), Upper mantle structure beneath the Azores hotspot from finite-frequency seismic tomography, *Earth Planet. Sci. Lett.*, *250*, 11–26.
- Yu, D., D. Fontignie, and J. G. Schilling (1997), Mantle plume-ridge interactions in the central North Atlantic: A Nd isotope study of Mid-Atlantic Ridge basalts from 30°N to 50°N, *Earth Planet. Sci. Lett.*, *146*, 259–272.